Hybrid Receive Beamforming

Applied to Ultrasound Imaging

by

Han Xu

B.Sc., University of Texas at San Antonio, 2022.

A Project Submitted in Partial Fulfillment of the Requirements for the Degree of

Master of Engineering

in the Department of Electrical and Computer Engineering.

University of Victoria

Hybrid Receive Beamforming

Applied to Ultrasound Imaging

by

Han Xu

B.Sc., University of Texas at San Antonio, 2022.

Supervisory Committee

Dr. Daler Rakhmatov, Department of Electrical and Computer Engineering

Supervisor

Dr. Mihai Sima, Department of Electrical and Computer Engineering

Departmental Member

Abstract

In the field of ultrasound imaging, reducing the computational cost of image reconstruction (i.e., applying receive beamforming to multichannel transducer data) is important for practical system implementations. Image quality is also crucial, which typically calls for the use of computationally intensive adaptive beamformers. This project aims to combine the advantages of low-complexity non-adaptive delay-and-sum (NA-DAS) beamforming and high-resolution minimum variance delay-and-sum (MV-DAS) adaptive beamforming. For this purpose, we propose a hybrid approach. First, our method utilizes NA-DAS beamforming to obtain a baseline image. Next, it detects regions of interest in the baseline image. Then, it applies MV-DAS beamforming to the detected regions and merges the result with the NA-DAS data to create a hybrid image. The proposed method was evaluated on four open-access experimental datasets (two focused imaging cases and two plane wave imaging cases). As expected, image resolution inside target regions improved, while the overall beamforming cost remained relatively low.

Table of Contents

Supervisory Committee……..……..ii

Abstract……..…….. iii

Table of Contents…….……..……. iv

List of Tables……..……..vi

List of Figures…….…….……...vii

Acknowledgements……...……...…….x

Dedication…….……... xi

List of Acronyms…….……... xii

Chapter 1: Introduction and Background……1

1.1 Ultrasound Imaging……1

1.1.1 Plane Wave Imaging…….3

1.1.2 Focused Imaging…….. 4

1.2 Receive Beamforming Background…… 5

1.2.1 Non-Adaptive Delay-and-Sum (NA-DAS) Beamformer…….5

1.2.2 Adaptive Minimum Variance Delay-and-Sum (MV-DAS) Beamformer…….7

1.3 Report Contribution and Organization……9

Chapter 2: Proposed Method…… 10

2.1 Step 1: NA-DAS Beamforming…… 11

2.2 Step 2: ROI Detection……... 12

2.2.1 Darker-Than-Background Object Detection…….. 12

2.2.2 Brighter-Than-Background Object Detection……17

2.2.3 Combining DTB and BTB Regions……... 20

2.3 Step 3: MV-DAS Beamforming……22

2.4 Step 4: Merging……24

2.4.1 Energy-Based (L2) Merging…….. 25

2.4.2 Intensity-Based (L1) Merging……26

2.4.3 Dynamic-Range-Based (DR) Merging……...27

2.4.4 Summary…… 29

Chapter 3: Evaluation Results……..31

3.1 Case 1 (Focused Imaging)……31

3.2 Case 2 (Plane Wave Imaging)……... 41

3.3 Case 3 (Plane Wave Imaging)……... 49

3.4 Case 4 (Focused Imaging)……53

3.5 Summary……... 57

Chapter 4: Conclusion and Future Work…… 59

4.1 Conclusion……59

4.2 Future Work……...60

Bibliography…….. 62

List of Tables

Table 3.1: Runtime comparison in Case 1..... 40

Table 3.2: Runtime comparison in Case 2..... 47

Table 3.3. Runtime comparison in Case 3..... 52

Table 3.4: Runtime comparison in Case 4..... 56

Table 3.5: Comparative Summary..... 57

List of Figures

Figure 1.1: Block diagram of an ultrasound imaging system [10,15]……. 2

Figure 1.2: (a) Conventional focused imaging, (b) ultrafast plane wave imaging [16]……...4

Figure 1.3: Block diagram of the conventional DAS beamformer [17]……..... 7

Figure 2.1: Proposed method diagram……... 10

Figure 2.2: Image binarization. From left to right: Original image, Binary image……... 13

Figure 2.3: Binary image after dilation……..14

Figure 2.4: Binary image after filling holes, clearing borders and image complement…….15

Figure 2.5: Final binary image……...16

Figure 2.6: Detected region and its bounding box…….17

Figure 2.7: K-means clustering. From left to right: Original image, Binary image after K-means clustering……18

Figure 2.8: Binary image after applying active contour segmentation……..19

Figure 2.9: Overlapping regions before and after merging……20

Figure 2.10: From left to right: Original image, DTB object detection image, BTB object detection image……..21

Figure 2.11: NA-DAS and MV-DAS beamforming output comparison for given ROI patches... 23

Figure 2.12: Hybrid image after direct patch substitution……24

Figure 2.13: Hybrid image after L2 merging…….26

Figure 2.14: Hybrid image after L1 merging…….27

Figure 2.15: Hybrid image after DR merging……28

Figure 2.16: Comparison of three merging methods. From top to bottom: L2 merging, L1 merging, DR merging……30

Figure 3.1: Case 1 beamforming results. From left to right: NA-DAS image, MV-DAS image, Hybrid image…… 32

Figure 3.2: Horizontal and vertical cross-sections at midpoint of bounding box A…….. 33

Figure 3.3: Horizontal cross-section comparison (Case 1, bounding box A)…… 34

Figure 3.4: Vertical cross-section comparison (Case 1, bounding box A)……..34

Figure 3.5: Lateral FWHM comparison (Case 1, bounding box C)…….. 36

Figure 3.6: Horizontal and vertical cross-sections at midpoint of bounding box B…….. 37

Figure 3.7: Horizontal cross-section comparison (Case 1, bounding box B)…… 38

Figure 3.8: Vertical cross-section comparison (Case 1, bounding box B)……..38

Figure 3.9: From top to bottom: Lateral and axial FWHM comparisons (Case 1, bounding box B)……39

Figure 3.10: Case 2 beamforming results. From left to right: NA-DAS image, MV-DAS image, Hybrid image…… 41

Figure 3.11: Horizontal and vertical cross-sections at midpoint of bounding box A…… 42

Figure 3.12: Horizontal cross-section comparison (Case 2, bounding box A)…….. 43

Figure 3.13: Vertical cross-section comparison (Case 2, bounding box A)……...43

Figure 3.14: Contrast ratio comparison (Case 2, bounding box A)……... 44

Figure 3.15: Horizontal and vertical cross-sections at midpoint of bounding box B…… 45

Figure 3.16: Horizontal cross-section comparison (Case 2, bounding box B)…….. 46

Figure 3.17: Vertical cross-section comparison (Case 2, bounding box B)……...46

Figure 3.18: Contrast ratio comparison (Case 2, bounding box B)……... 47

Figure 3.19: Case 3 beamforming results. From left to right: NA-DAS image, MV-DAS image, Hybrid image……. 49

Figure 3.20: Zoom-in section comparison. From top to bottom: NA-DAS image, MV-DAS image, Hybrid image……. 51

Figure 3.21: Case 4 beamforming results. From left to right: NA-DAS image, MV-DAS image, Hybrid image……. 53

Figure 3.22: Zoom-in section comparison. From top to bottom: NA-DAS image, MV-DAS image, Hybrid image……..... 55

Acknowledgements

I would like to thank my supervisor, Dr. Daler Rakhmatov, express my deepest gratitude for his unwavering encouragement, support and guidance during my master's studies. Furthermore, I would like to thank Dr. Mihai Sima, my supervisory committee member, for his valuable support in the further development of my project.

Dedication

This work is dedicated to my family and friends.

List of Acronyms

Brighter-Than-Background [Object Detection]	BTB
Coherent Plane Wave Compounding	CPWC
Computerized Imaging Reference Systems [Phantom]	CIRS
Contrast Ratio	CR
Darker-Than-Background [Object Detection]	DTB
Delay-and-Sum [Beamforming]	DAS
Dynamic Range	DR
Focused Imaging	FI
Full Width at Half-Maximum	FWHM
Minimum Variance [Adaptive Beamforming]	MV
Minimum Variance Delay-and-Sum [Adaptive Beamforming]	MV-DAS
Non-adaptive [Beamforming]	NA
Non-adaptive Delay-and-Sum [Beamforming]	NA-DAS
Plane Wave	PW

Plane Wave Imaging	PWI
Region of Interest	ROI
Ultrasound Toolbox	USTB

Chapter 1

Introduction and Background

1.1 Ultrasound Imaging

Ultrasound imaging is a core diagnostic tool in medical practice and is known for its non-invasive nature and versatility in visualizing soft tissue, organs, and blood flow in real time. The development of ultrasound technology has been significantly influenced by advances in beam shaping techniques, which are critical to improving image quality and diagnostic accuracy [1]. In the field of medical imaging, especially software-controlled ultrasound imaging, the sophistication and effectiveness of relevant signal processing are crucial for creating high-quality diagnostic images [10]. The path of an ultrasound signal from transmission to image display involves several steps as shown in Fig. 1.1.

The ultrasound imaging system process begins with the transmit beamformer directing the pulser to generate timed electrical signals supplied to the ultrasound transducer via the transmit/receive switch. Typically, multiple transducer elements are activated during transmission in order to create a desired transmit beam pattern and to increase the signal-to-noise ratio. The transducer converts the electrical signals into ultrasound waves, which travel through the body and reflect off tissues. The reflected waves are received by the transducer and converted back into electrical signals, which are then directed to the receiver. These signals undergo time gain compensation and receive beamforming (focusing) [15,39]. The beamformed signals are then processed using envelope detection, log compression, and display preprocessing. The resulting

data is converted into a scan format, further enhanced by the postprocessor, and finally displayed as an image on the display.

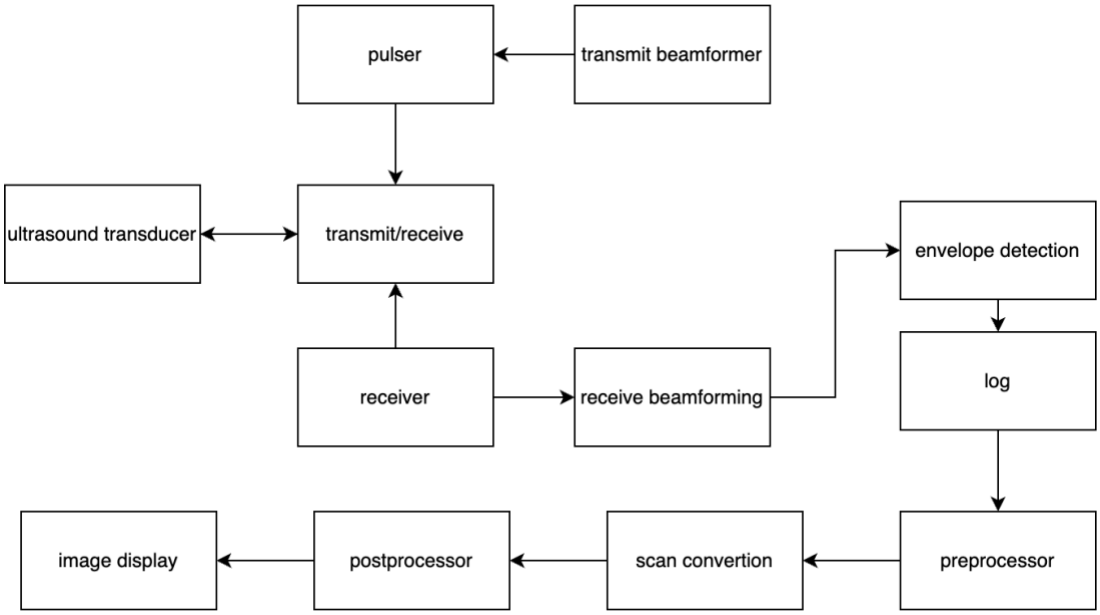

Figure 1.1: Block diagram of an ultrasound imaging system [10,15].

When transmitting, a probe emits ultrasound waves that propagate through the body at a speed that is typically assumed to be 1540 m/s [11]. After transmission, the same probe receives echoes reflected from different tissues. It must wait for the echoes to return before emitting another wave, which limits the imaging frame rate [11]. The quality of the ultrasound image is improved by using a focused transmit beam (transmit beamforming) coupled with dynamic receive focusing (receive beamforming) [11].

Advances in ultrasound technology have explored unfocused transmissions using plane-wave or divergent-wave beams. These unfocused waveforms produce reflections that can be combined after capture to simulate a focused beam transmission, which is known as coherent

compounding [26,27]. This modern approach enables more flexible and faster imaging processes, which are critical for effective diagnostic applications [11].

1.1.1 Plane Wave Imaging

Coherent Plane Wave Compounding (CPWC) represents a significant advance in medical imaging technology, as highlighted in [12]. In conventional (focused) ultrasound imaging, the transmitted waves focus on a target at a specific depth for each sequentially imaged scan line, as shown in Fig. 1.2(a). This results in high-quality image sections in the target area, but not elsewhere in the image. In contrast, the CPWC technique uses planar transmissions to achieve very high data acquisition rates (in order of thousands of raw data frames per second), a critical feature for applications such as Doppler imaging of blood flow or transient elastography. By illuminating a large area of interest with a single transmission, plane wave imaging dramatically reduces the number of transmissions required, as shown in Fig. 1.2(b). While individual plane wave images typically suffer from lower contrast and resolution, coherently combining multiple images obtained from several plane wave transmissions at different angles can significantly improve image quality, rivaling that of fully focused techniques [1,12,13]. However, this method faces challenges, such as the sensitivity to motion between transmissions and the presence of “edge waves” that occur outside the central region where the plane wave assumption is valid. These factors can degrade image quality, highlighting the complexity and trade-offs in plane wave imaging [1,12,13].

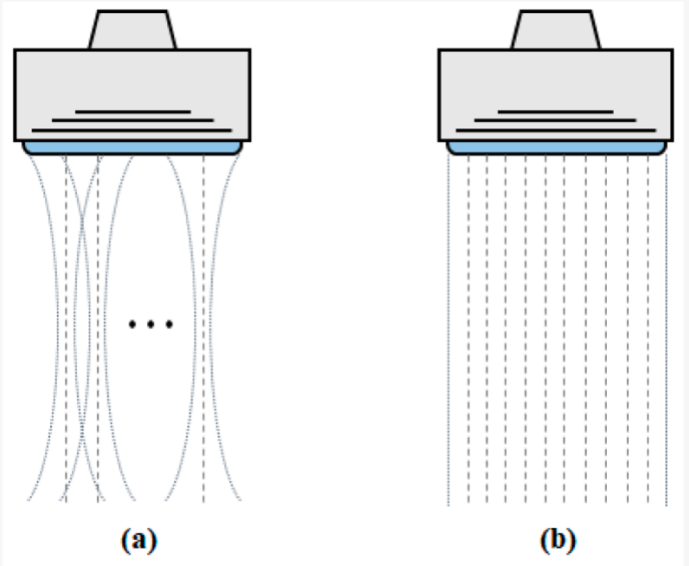

Figure 1.2: (a) Conventional focused imaging, (b) ultrafast plane wave imaging [16].

1.1.2 Focused Imaging

Focused Imaging (FI) is a traditional and widely used approach in ultrasound technology in which the ultrasound waves from individual transducer elements converge at a specific focal point before diverging. This method remains the predominant transmission technique in modern ultrasound systems [1,11]. In focused imaging, each transmit event yields a single scan line in the resulting image, typically requiring dozens to hundreds of transmissions to create a complete image. However, it offers significant advantages in the field of nonlinear acoustics, particularly in second harmonic imaging. The higher peak pressures achieved through focused transmissions in the body lead to stronger nonlinear effects and thereby increase second harmonic generation [28]. This capability not only improves image quality but also provides superior contrast compared to other methods such as Plane Wave (PW), Diverging Wave (DW) and Synthetic Transmit Aperture (STA) imaging, making focused imaging a crucial tool in the advanced medical diagnostics [1].

1.2 Receive Beamforming Background

Receive beamforming, the method by which the signals from multiple transducer elements are processed to produce a coherent image, has evolved from simple analog implementations to sophisticated digital and software-based approaches [22,23]. In recent years, software beamforming has become a transformative technology in ultrasound imaging. Unlike traditional methods that rely on fixed hardware to direct and focus ultrasound beams, software beamforming uses advanced algorithms to dynamically manipulate echo signals. This shift allows for finer control of image resolution and contrast, enabling detailed visualization even in complex diagnostic scenarios [22].

In this project, we explore two basic variants of delay-and-sum (DAS) receive beamforming: conventional non-adaptive (NA-DAS) and minimum variance (MV-DAS) adaptive techniques. Details are described in the following sections. We applied and evaluated these receive beamformers in both focused imaging and plane wave imaging scenarios (see Chapter 3).

1.2.1 Non-Adaptive Delay-and-Sum (NA-DAS) Beamformer

Delay-and-sum (DAS) beamforming is a fundamental signal processing technique widely used in applications such as ultrasound imaging. This method involves delaying and summing received signals to enhance the desired signal from a particular direction while minimizing noise and interference from other directions [18,24,25].

DAS beamforming works by applying time delays to the signals received from each element in an array to align them in phase for a particular direction or focal point. This alignment

creates constructive interference for signals originating from the desired direction, while causing destructive interference for others, producing a beam in a specific direction or point [1].

In a conventional DAS beamformer as shown in Fig. 1.3, the input signals $s_0(t), s_1(t), \ldots, s_{M-1}(t)$ are delayed by specific amounts $\tau_0, \tau_1, \ldots, \tau_{M-1}$, which are determined based on the distances traveled by the transmitted and reflected waves relative to the pixel position specified by the vector $\vec{r}_p$, or equivalently by the (x_p, z_p) coordinates of that pixel. These delayed signals are then multiplied by the corresponding weights $w_0, w_1, \ldots, w_{M-1}$, which can be either fixed or adaptive. Fixed weights are often derived from window functions such as rectangular, Hamming, or boxcar windows [19]. The window choice directly impacts the trade-off between the mainlobe width and the sidelobe level, influencing image quality in terms of resolution and contrast. Adaptive weights, on the other hand, adjust dynamically based on the incoming data, potentially providing better performance in varying conditions. The weighted signals are summed to construct the output signal $b(\vec{r}_p)$.

Thus, the conventional DAS implementation is the coherent combination of the signal values received by all elements [2]:

$$b_{DAS} = \sum_{m=0}^{M-1} w_m s_m, \tag{1.1}$$

where M is the number of elements, s_m is a delayed signal from element m, and w_m is the receive apodization weight, which is fixed in the NA-DAS case. Equation (1.1) can be written in algebraic form as [2]

$$b_{DAS} = w^H s. \tag{1.2}$$

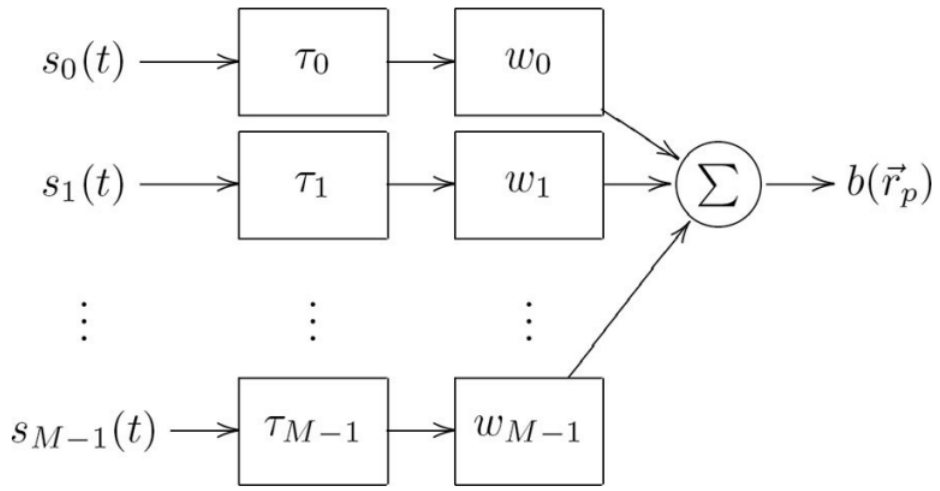

Figure 1.3: Block diagram of the conventional DAS beamformer [17].

1.2.2 Adaptive Minimum Variance Delay-and-Sum (MV-DAS) Beamformer

To achieve a narrow mainlobe width while dramatically reducing the sidelobe level (leading to both image resolution and contrast improvements), adaptive beamforming can be used. In this project, we use the minimum variance delay-and-sum (MV-DAS) beamformer [13,17]. Unlike the NA-DAS beamformer, which uses fixed weights, the MV-DAS beamformer calculates the weights dynamically, based on the covariance matrix of the received signals. By minimizing the variance of the beamformed signal, the MV-DAS beamformer achieves superior spatial resolution and better interference rejection compared to conventional beamforming techniques [30,31]. However, this comes with increased computational complexity as real-time estimation of the covariance matrix and its inversion are required.

The MV-DAS beamformer stems from Capon's method of computing data-dependent weights that minimize output variance while maintaining unity gain in the steering direction [3,13,17,29,40]. This is posed as the following optimization problem:

$$min_w E|b_{DAS}|^2 = w^H R w, \text{ subject to } w^H s = a, \qquad (1.3)$$

where the spatial covariance matrix is represented by $R \equiv E\{ss^H\}$, the expected value operator is denoted by E, and the steering vector has the value $a = 1$. Using the Lagrange multiplier method [3], the solution to problem (1.3) is given by

$$w_{MV} = \frac{R^{-1}a}{a^H R^{-1} a}. \qquad (1.4)$$

The spatial covariance matrix is typically unknown, but it can be estimated for point (x, z), assuming a linear array, as follows [3]:

$$\tilde{R}(x,z) = \frac{\sum_{k=-K}^{K} \sum_{I=0}^{M-L} \bar{s_l}(x,z-k) \bar{s_l}^H(x,z-k)}{(2K+1)(M-L+1)}, \qquad (1.5)$$

where L is the length of the subarray, (2K+1) is the number of axial samples, and

$$\bar{s_l}(x,z) = [s_i(x,z) \;\; s_{i+1}(x,z) \;\; \cdots \;\; s_{i+L-1}(x,z)]^T. \qquad (1.6)$$

The subarray averaging in equation (1.5) is commonly used to improve robustness. Also, diagonal loading is commonly added to the estimated covariance matrix: $\tilde{R}(x,z) = \hat{R}(x,z) + \epsilon I$, where

$$\epsilon = \frac{\Delta}{L} tr\{\hat{R}(x,z)\}, \qquad (1.7)$$

which further increases numerical stability. Then, the beamformed output is computed as

$$b_{MV} = \frac{1}{M-L+1} \sum_{I=0}^{M-L} w_{MV}^H \bar{s_l}. \qquad (1.8)$$

In our case of MV-DAS beamforming, L was set to 50% of the active receive channels, $K = 1.5\lambda$, and a diagonal loading factor of $\Delta = 1/100$ was used as suggested in [1].

1.3 Report Contribution and Organization

This project is inspired by the previous work [14] that proposed a hybrid beamforming technique that combined non-adaptive and adaptive methods to produce high-quality ultrasound images at low computational cost. Their approach involved automatically switching between NA-DAS as a non-adaptive method and an adaptive method, such as the Generalized Sidelobe Canceller (GSC) and the Adaptive Single Snapshot Beamformer (ASSB), based on the input coherence factor (CF). Whenever the CF value of a properly delayed input vector exceeded some threshold, the summation was done adaptively; otherwise, the delayed signals were summed non-adaptively.

This project aims to develop another hybrid approach that combines the benefits of NA-DAS and MV-DAS beamforming in a different way. First, we use the NA-DAS method to obtain an entire image, which is used as a baseline to detect regions of interests (ROIs) to be enhanced by adaptive beamforming. Then, the MV-DAS method is applied to each detected ROI to increase image quality within the boundaries of that ROI. In other words, our approach avoids using expensive adaptive beamforming outside ROIs, thus reducing the overall computational cost while achieving high resolution inside ROIs.

The rest of the report is organized as follows. Chapter 2 describes our proposed hybrid beamforming method. Chapter 3 presents the evaluation results for the NA-DAS, MV-DAS, and hybrid beamformers applied to four open-access experimental datasets (two PWI and two FI cases). Finally, Chapter 4 provides our concluding remarks and outlines possible future work directions.

Chapter 2

Proposed Method

This project implementation is based on the Ultrasound Toolbox (USTB) [1,11]. This toolbox (https://www.USTB.no) is an open-source processing framework facilitating the comparison of imaging techniques and the dissemination of research results. The main aim of the USTB is to provide a unified platform for comparing different imaging and beamforming methods while promoting the exchange of relevant data sets and algorithms.

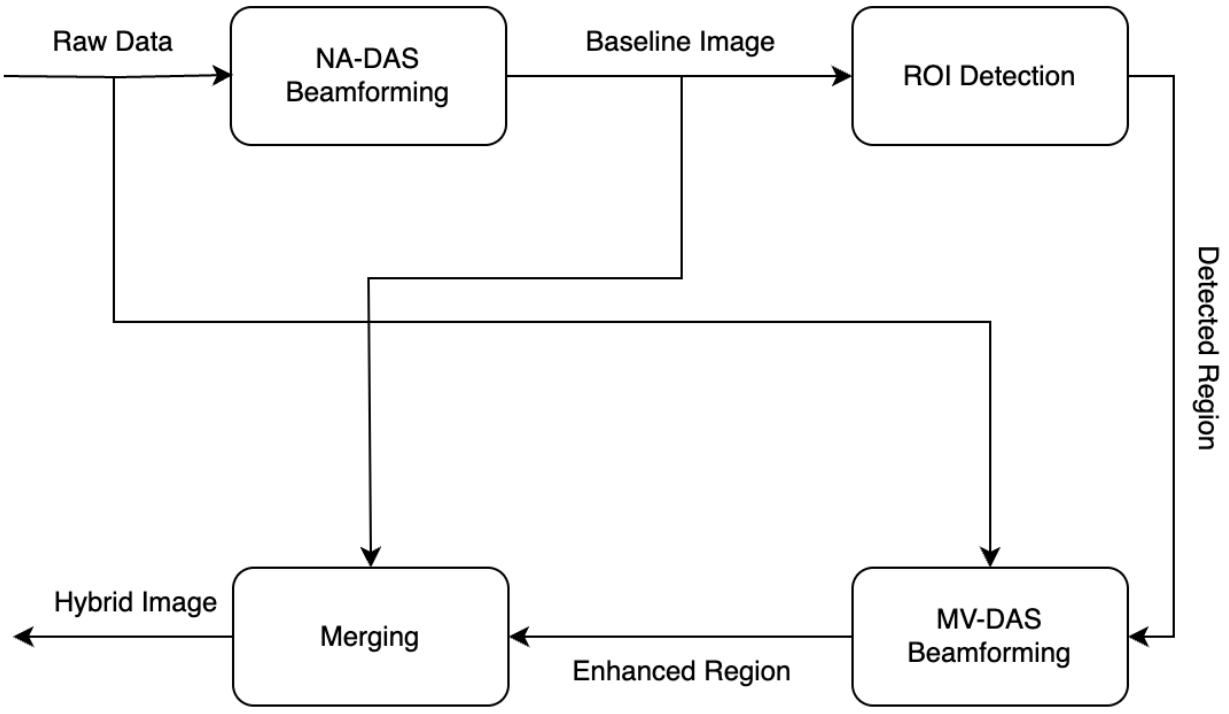

Figure 2.1: Proposed method diagram.

The proposed method includes four main steps to compute a hybrid image from the raw channel data, as shown in Fig. 2.1. We obtain the hybrid image by combining the outputs of both non-adaptive (NA-DAS) and adaptive (MV-DAS) beamforming described in Chapter 1. We use the relatively inexpensive NA-DAS beamformer to obtain a baseline image in its entirety, but we also apply the more expensive MV-DAS beamformer to specific regions of interest that are detected automatically. In other words, adaptive beamforming is applied selectively, to enhance resolution only in specific regions.

2.1 Step 1: NA-DAS Beamforming

The first step is to apply NA-DAS beamforming to obtain a baseline image. The input includes the raw channel data and the receive apodization parameters. The output is a non-adaptive image, i.e., our baseline computed by a conventional non-adaptive beamformer.

The receive apodization parameters are the so-called F-number and the window function (weights) used during summation of delayed signals. The F-number is the ratio of imaging depth z to the aperture width D, which is kept constant during receive beamforming. At smaller z (i.e., closer to the surface), D is made smaller as well, which means that fewer delayed signals contribute to the sum. By using such "dynamic receiving aperture", image artifacts are reduced [41,42]. The apodization window refers to the mathematical function specifying the weights applied to the received signals across the transducer elements, as described in Chapter 1 [19]. The boxcar window and the F-number of 1.5 have been used in the NA-DAS case. This choice simplifies the beamforming process and provides a reasonable balance between resolution and depth of field for consistent image quality.

2.2 Step 2: ROI Detection

The second step is to detect the regions of interest and create bounding boxes around them. The input is the NA-DAS beamformed data from the previous step and the output is the detected regions. To detect both dark and bright regions, we employ two methods. One of them detects Darker-Than-Background (DTB) objects, while the other detects Brighter-Than-Background (BTB) objects.

Before applying these two methods, some preprocessing of the NA-DAS beamformed data is required. First, the NA-DAS beamformed data envelope is computed. By applying normalization to the envelope, where each value is scaled relative to the maximum, we restrict the data to the range [0,1]. Finally, the contrast of our normalized envelope image is enhanced by saturating the bottom 1% and top 1% of all pixel values.

2.2.1 Darker-Than-Background Object Detection

To detect Darker-Than-Background (DTB) objects, we convert the 2D grayscale envelope image into a binary image using adaptive thresholding. It calculates locally adaptive threshold levels using first-order image statistics around each pixel. Such thresholding is controlled by the sensitivity parameter σ, specified as a number in the range [0, 1]. A higher sensitivity value leads to thresholding more pixels as an object [20,21]. In this work, we set the sensitivity parameter σ to 0 for all cases. By doing this, the process is simplified to a standard thresholding approach, which is computationally less intensive. Fig. 2.2 shows the result of image binarization for this section's running example.

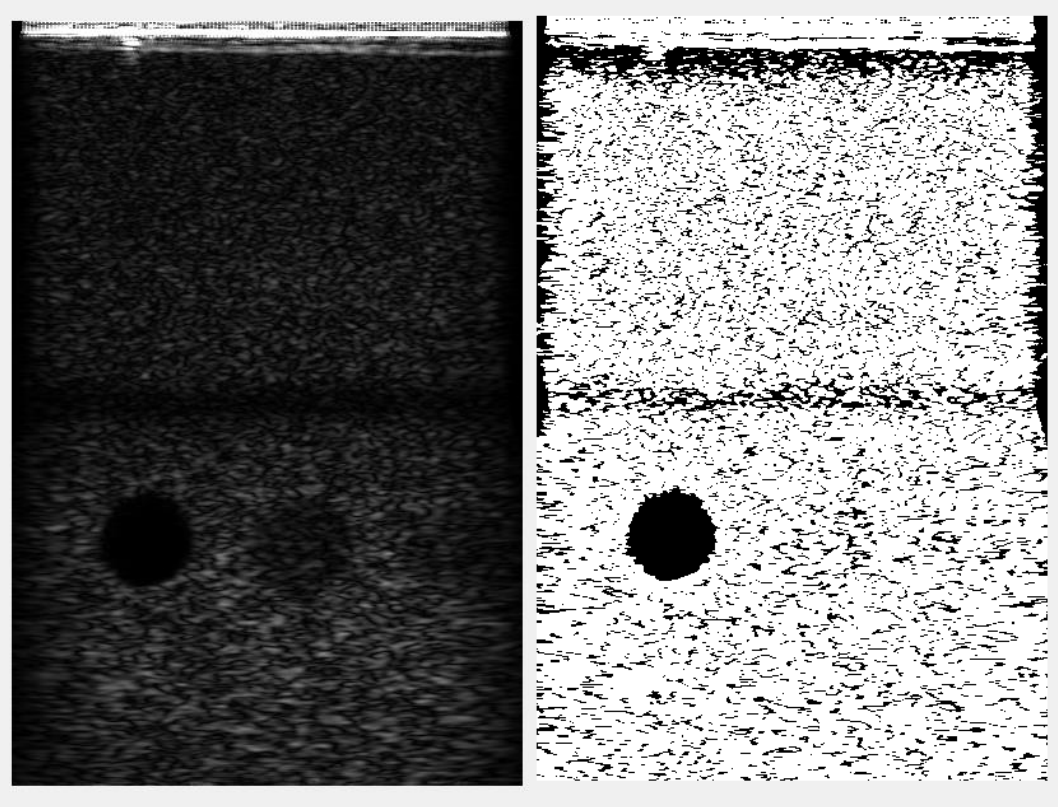

Figure 2.2: Image binarization. From left to right: Original image, Binary image.

To reduce noise, we use the dilation operation that "grows" or "thickens" objects in a binary image. The specific manner and extent of this thickening is controlled by a structuring element [32,33]. The binary dilation of A by B, denoted $A \oplus B$, is defined as the set operation:

$$A \oplus B = \left\{ z \middle| (\hat{B})_z \cap A \neq \emptyset \right\}, \tag{2.1}$$

where $\emptyset$ is the empty set and B is the structuring element. In words, the dilation of A by B is the set consisting of all the structuring element origin locations where the reflected and translated $\hat{B}$ overlaps at least some portion of A [6]. As our structuring element we use a disk having some specified radius ρ. In this work, radius ρ is set to 3 pixels, which corresponds to 0.3 mm in our beamforming grid. Fig. 2.3 show the result of applying the dilation operation to the binary image from Fig. 2.2.

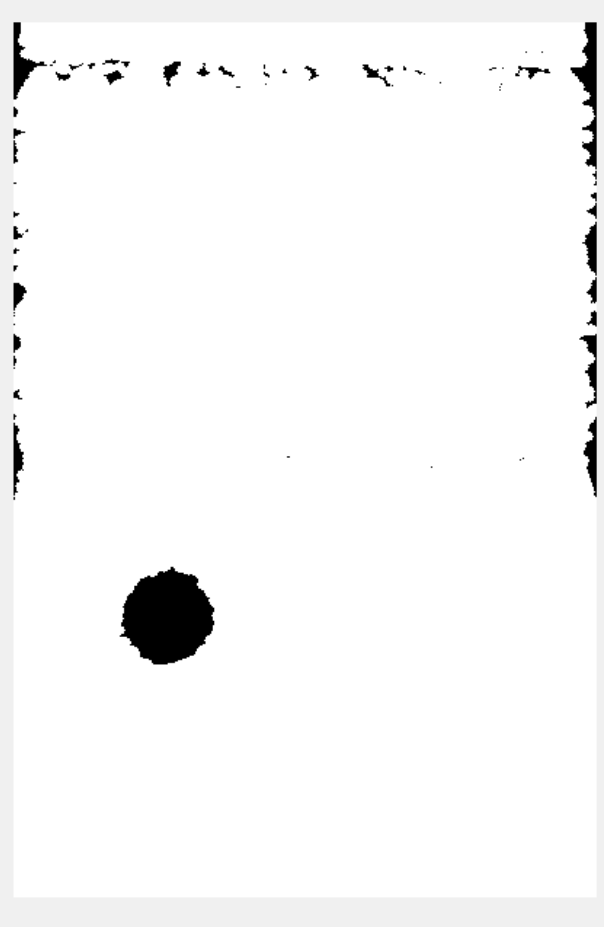

Figure 2.3: Binary image after dilation.

Although dilation significantly reduces noise in the binary image, it is still insufficient. Next, we apply two additional morphological techniques: clearing the border and filling holes [7,34,35]. They remove objects touching the image border and fill small holes, resulting in a less fragmented region representation. Then, we perform image complementation, whereby zeros become ones and ones become zeros. The resulting image is shown in Fig. 2.4.

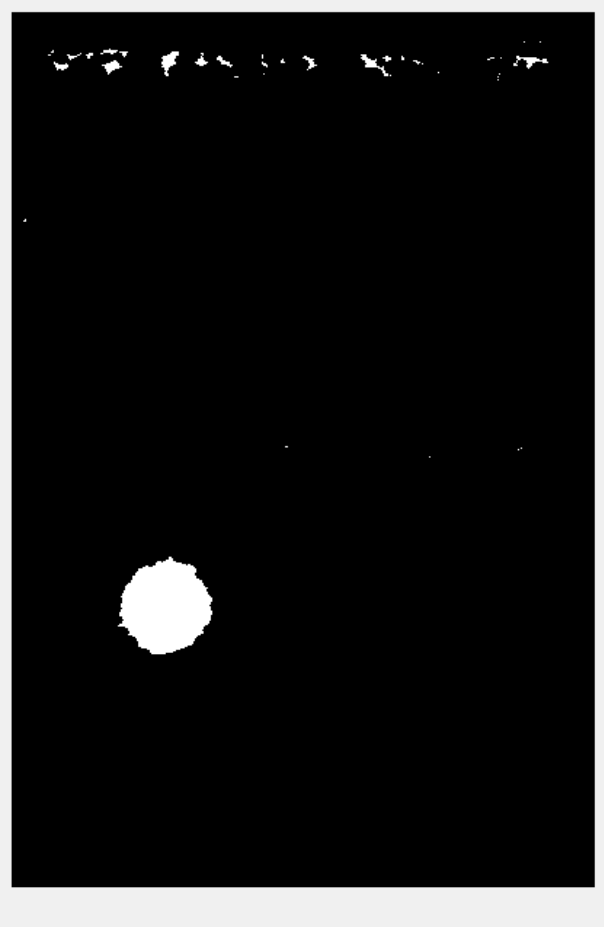

Figure 2.4: Binary image after filling holes, clearing borders and image complement.

Finally, our proposed method discards smaller regions and retains only larger ones, measured by the number of pixels they contain. There are two parameters for the area threshold: the minimum area A_{min} and the maximum area A_{max}. By default, the maximum area is set to the total area of the image. The minimum area is adjustable according to the smallest region size that needs to be detected. In this work, A_{min} is set to 0.06% of A_{max}. The final image for this section's running example is shown in Fig. 2.5.

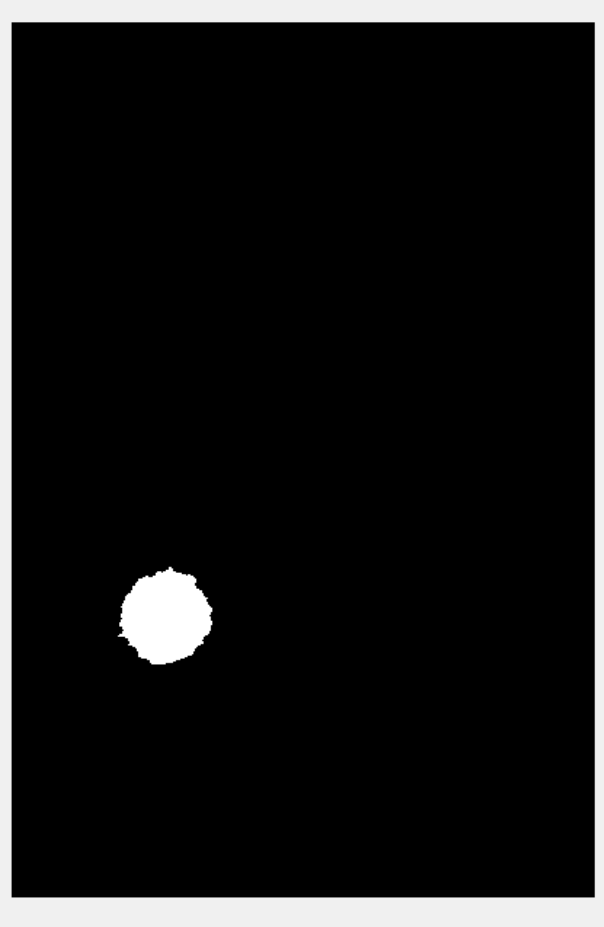

Figure 2.5: Final binary image.

After our DTB object detection, we represent the corresponding ROI using a bounding box, as illustrated in Fig. 2.6. Note that the bounding box boundaries are slightly extended by five wavelengths to include surrounding pixels. If any bounding boxes overlap, they are merged into a single bounding box that includes the contents of both original boxes while remaining within the image boundaries. An example of bounding box merging is shown in the next section.

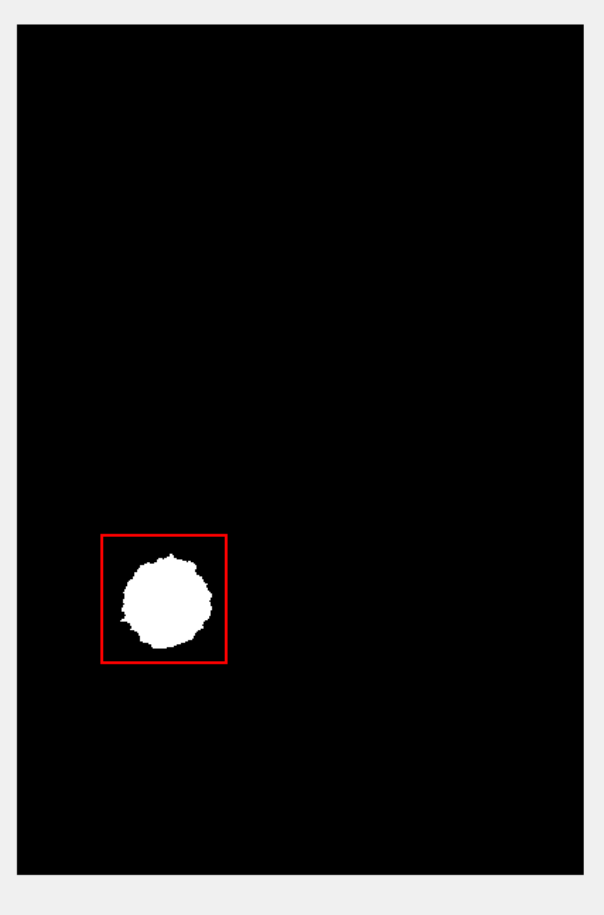

Figure 2.6: Detected region and its bounding box.

2.2.2 Brighter-Than-Background Object Detection

To detect Brighter-Than-Background (BTB) objects, we first apply K-means clustering to the 2D grayscale envelope image. K-means clustering is a technique used to segment digital images into K distinct regions by iteratively running the algorithm with various initial centroid positions [8]. The goal is to achieve an optimal partitioning by minimizing the overall distance between points and their respective cluster centroids. There are two parameters for this process: the number of clusters k and number of iterations n for repeated clustering. In this work, we use two clusters and perform two iterations for all cases.

Once the image is segmented, a binary mask is created to isolate one of the regions, enabling focused analysis on that specific segment. A running example of image binarization and K-means clustering is shown in Fig. 2.7.

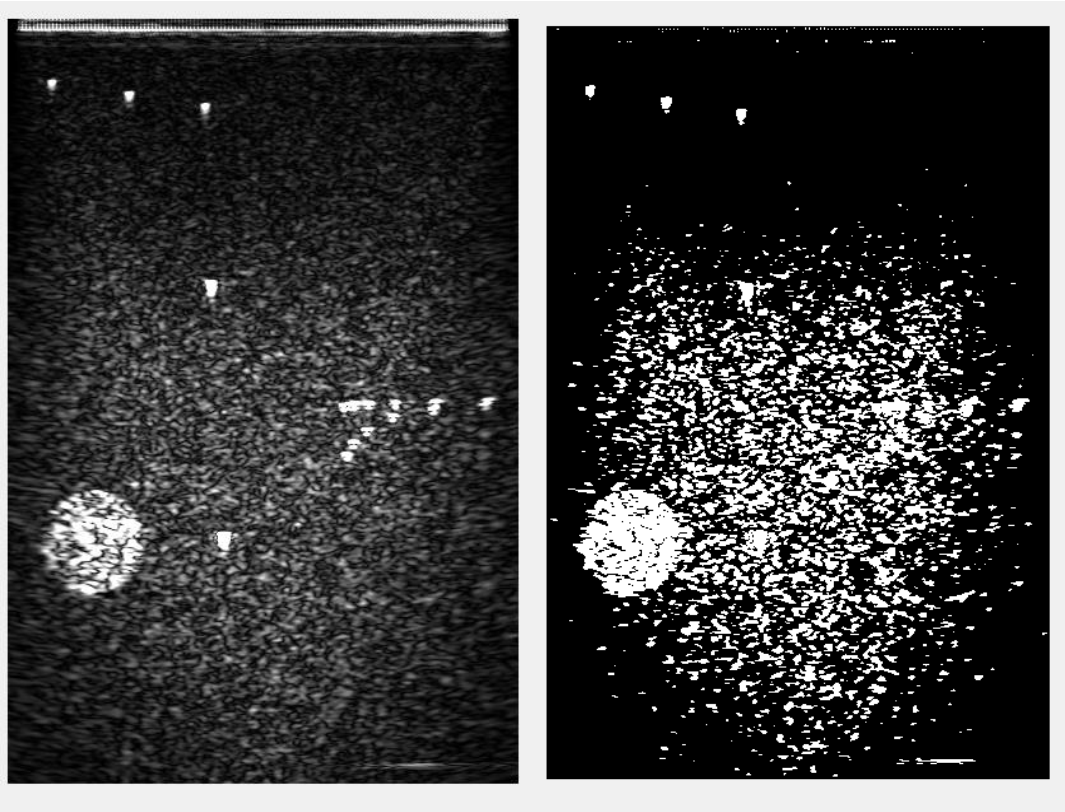

Figure 2.7: K-means clustering. From left to right: Original image, Binary image after K-means clustering.

After initial segmentation via K-means clustering, active contour segmentation is applied to refine object boundaries within the image. The active contours technique is an iterative region-growing image segmentation algorithm that specify initial curves on an image then use to evolve the curves towards object boundaries [9]. The inputs are the envelope image and the mask argument. The mask size must match the size of the image. The mask argument is a binary image

that specifies the initial state of the active contour. We employ "edge"-based active contour segmentation [38]. The active contour evolution stops when either the maximum number of iterations is reached, or the contour position in the current iteration matches the contour position in one of the most recent five iterations. By focusing on edges, the method allows the contour to seek out and align with significant changes in intensity or color, indicating object boundaries. In this work, the maximum number of iterations was set to 20 for all cases. The resulting image example is shown in Fig. 2.8.

Figure 2.8: Binary image after applying active contour segmentation.

The remaining steps follow the same procedure as in the DTB case. First, we discard smaller regions based on the number of pixels they contain. Next, we represent the corresponding ROIs using bounding boxes. Finally, we merge the overlapping bounding boxes. The resulting images before and after merging are shown in Fig. 2.9.

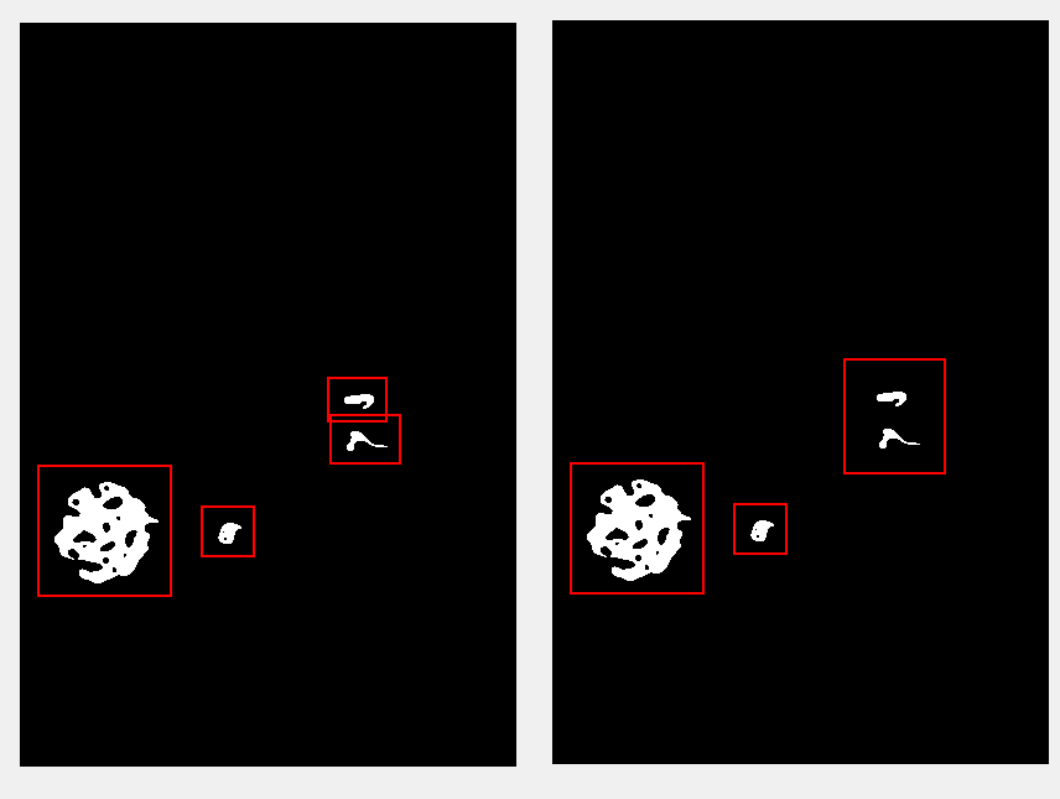

Figure 2.9: Overlapping regions before and after merging.

2.2.3 Combining DTB and BTB Regions

Before proceeding with further processing, we combine the ROIs identified by the DTB and BTB object detection methods to create a unified set of bounding boxes. To handle overlaps, we calculate the intersection area for all pairs of bounding boxes inside the unified set. If a pair of

boxes overlaps, we merge them to generate a new bounding box that covers the ROIs of both overlapping bounding boxes.

Fig. 2.10 provides an example of DTB and BTB object detection, illustrating the necessity of combining these methods. When only the BTB method is utilized, as illustrated in the rightmost image, some objects may be missed. Therefore, we employ both BTB and DTB object detection to enhance ROI coverage.

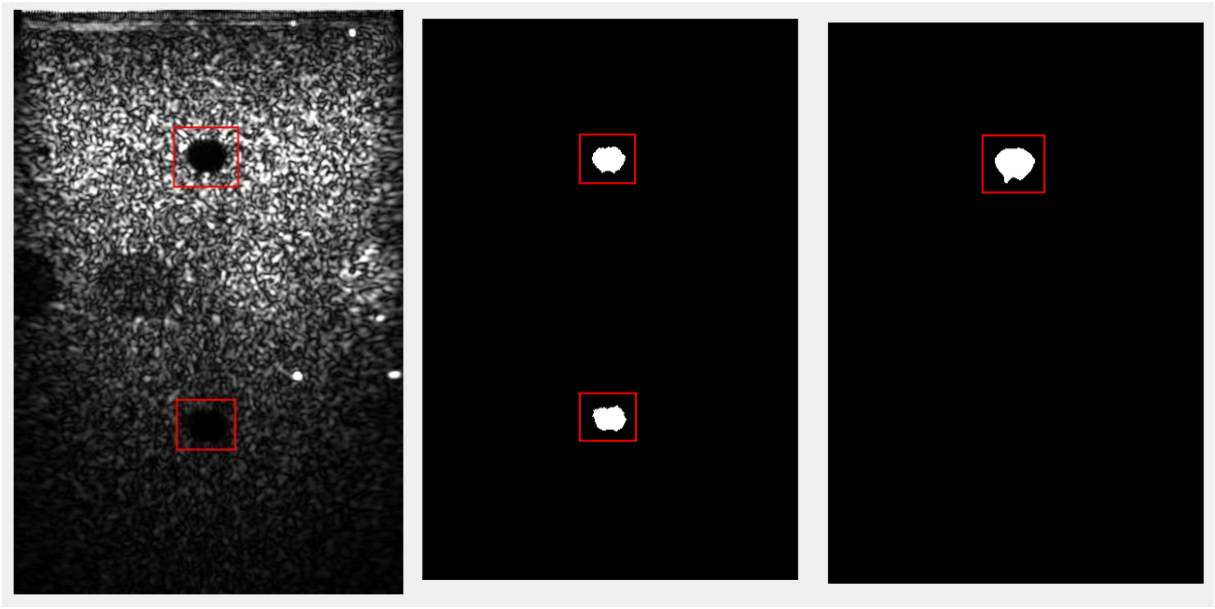

Figure 2.10: From left to right: Original image, DTB object detection image, BTB object detection image.

To summarize, the ROI detection in this project is performed automatically, utilizing several tunable parameters under the user's control. These parameters (mentioned in the preceding sections) include the threshold sensitivity (binarization), structuring element shape (dilation), number of clusters and iterations (K-means clustering and active contour segmentation), and minimum area threshold (small object exclusion). However, the ROI detection can also be

performed by the user interactively, by inspecting the baseline image and then selecting desired sections for subsequent enhancement via MV-DAS beamforming.

2.3 Step 3: MV-DAS Beamforming

The third step involves applying MV-DAS beamforming to the detected regions of interest. The bounding box coordinates define the image patches to be enhanced, and we apply adaptive MV-DAS beamforming to them. Its implementation is based on the USTB [1,11]. Two parameters are also used for MV-DAS beamforming: the window and the F-number, as detailed in Chapter 1. The F-number is 1.5 (as in the NA-DAS beamforming case), but the window is now computed adaptively. Fig. 2.11 provides a few examples comparing NA-DAS beamforming and MV-DAS beamforming for several detected ROI patches. As one can see, MV-DAS beamforming produces sharper peaks within the enhanced regions, indicating that the resolution is significantly improved compared to NA-DAS beamforming.

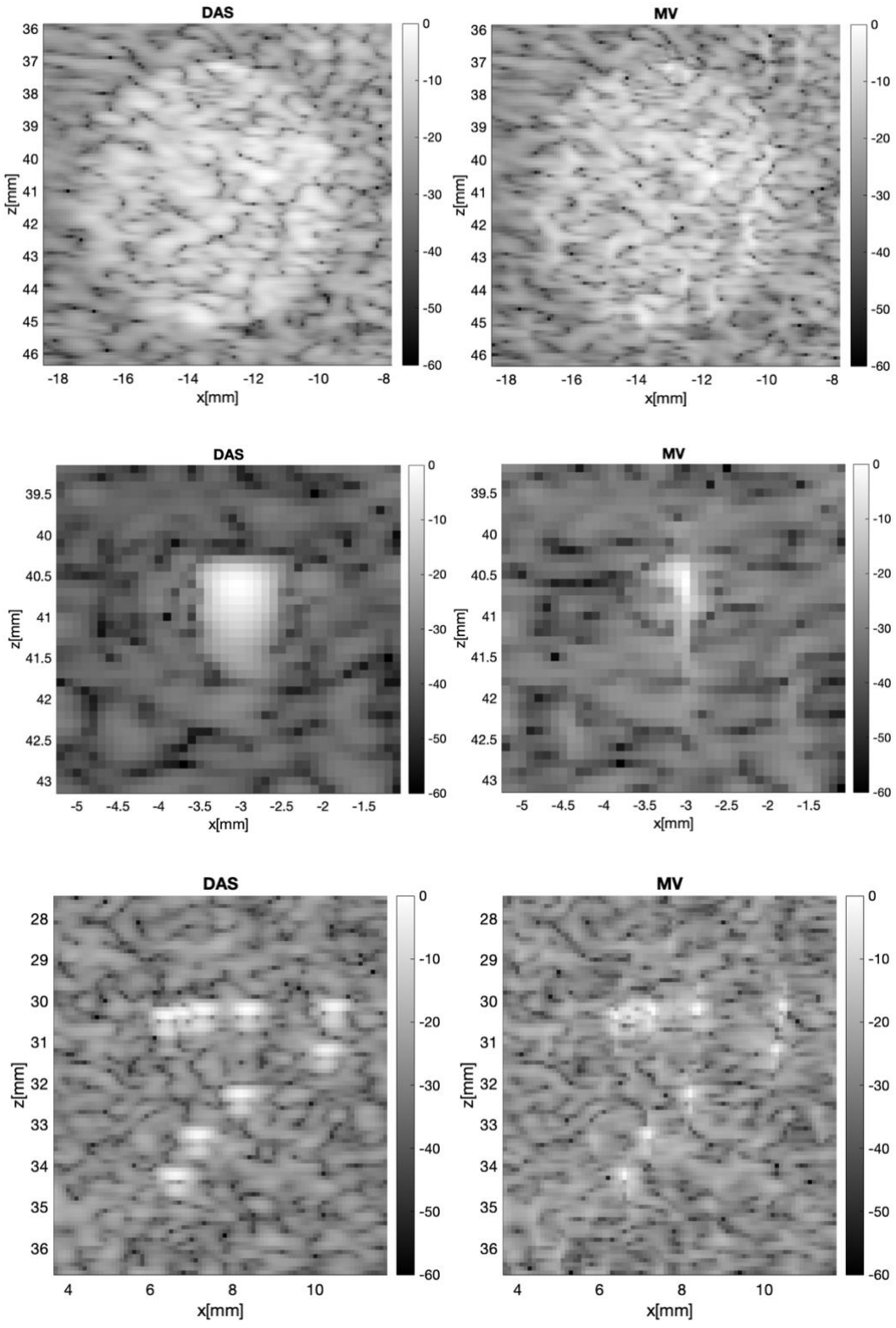

Figure 2.11: NA-DAS and MV-DAS beamforming output comparison for given ROI patches.

2.4 Step 4: Merging

The fourth step is to replace the NA-DAS beamformed ROI patches with the ones enhanced by MV-DAS beamforming, thus forming a hybrid image. However, direct substitution of an NA-DAS output with an MV-DAS output within a given ROI can result in a background mismatch. For example, a substituted image patch may appear slightly brighter than the overall background, which is not desirable, as shown in Fig. 2.12.

To address this issue, we replace the NA-DAS beamformed pixels with the MV-DAS beamformed pixels by adjusting the intensity of the latter using three different methods, described in the following three sections.

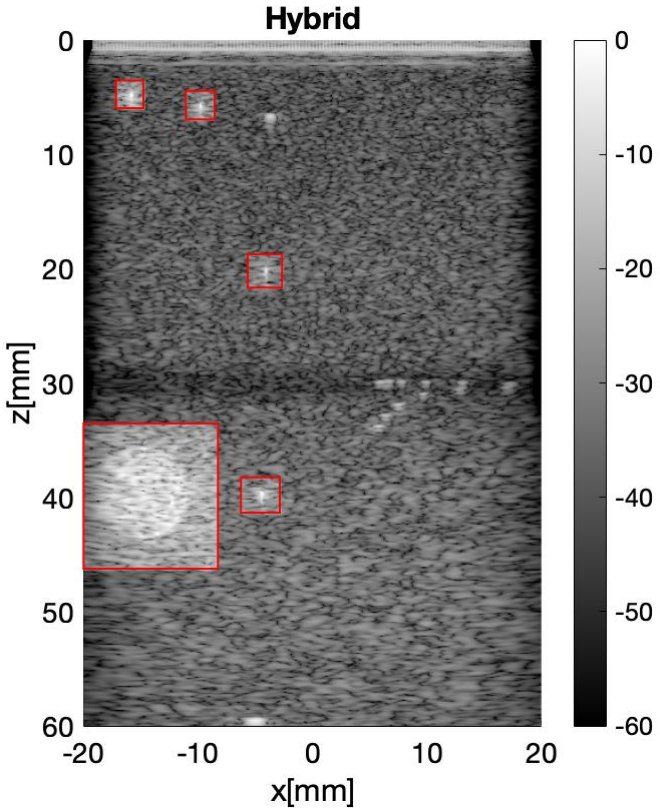

Figure 2.12: Hybrid image after direct patch substitution.

2.4.1 Energy-Based (L2) Merging

The first method relies on the total energy associated with a given ROI patch, computed as the sum of the absolute squared values of all constituent elements [37],

$$E_{NA} = \sum_{i=1}^{N} \left| b_i^{NA} \right|^2 \tag{2.1}$$

$$E_{MV} = \sum_{i=1}^{N} \left| b_i^{MV} \right|^2, \tag{2.2}$$

where E_{NA} is the total energy of the NA-DAS pixels, E_{MV} is the total energy of the MV-DAS pixels, b_i is the intensity (brightness) of pixel i within a patch, and N is the total number of pixels forming that patch. To compensate for any differences in energy levels, we introduce the scaling factor S_{L2}, given by

$$S_{L2} = \sqrt{E_{NA}/E_{MV}}. \tag{2.3}$$

The MV-DAS pixels are then multiplied by this scaling factor to adjust the corresponding ROI energy level to that of the NA-DAS pixels within the same ROI. The adjusted enhanced patches are then used to replace the corresponding target regions in the NA-DAS image. Fig. 2.13 demonstrates this approach using the same image example as in Fig. 2.12.

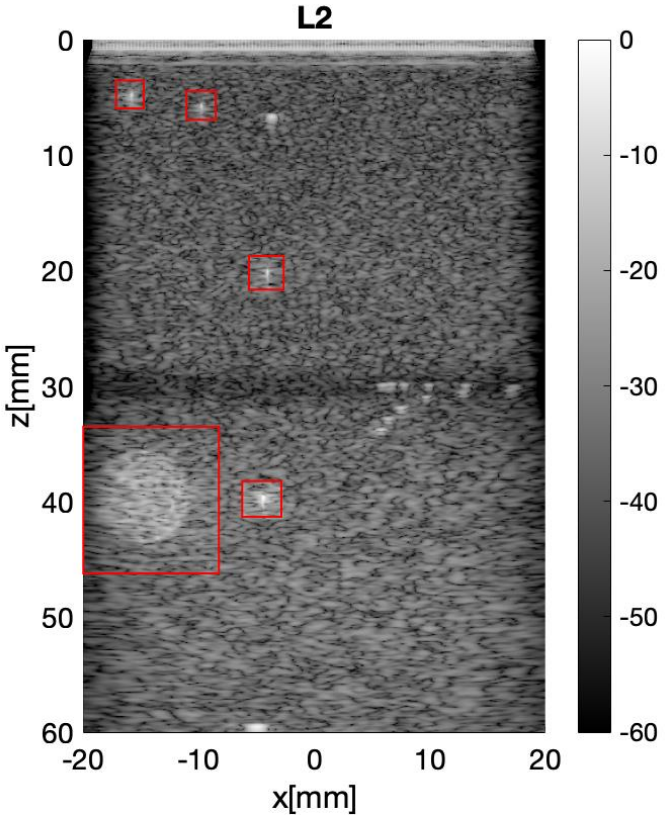

Figure 2.13: Hybrid image after L2 merging.

2.4.2 Intensity-Based (L1) Merging

In the second method, we use the sum of the absolute values of all elements within a given ROI [36], given by

$$I_{NA} = \sum_{i=1}^{N} \left| b_i{}^{NA} \right| \tag{2.4}$$

$$I_{MV} = \sum_{i=1}^{N} \left| b_i{}^{MV} \right|, \tag{2.5}$$

where I_{NA} is the total intensity of the NA-DAS pixels, I_{MV} is the total intensity of the MV-DAS pixels. The corresponding scaling factor becomes

$$S_{L1} = I_{NA}/I_{MV}. \tag{2.6}$$

Similar to the L2 merging method, the MV-DAS pixels are then multiplied by this scaling factor to achieve a proportional intensity representation in a hybrid image. This is illustrated in Fig. 2.14 obtained from the same running example image.

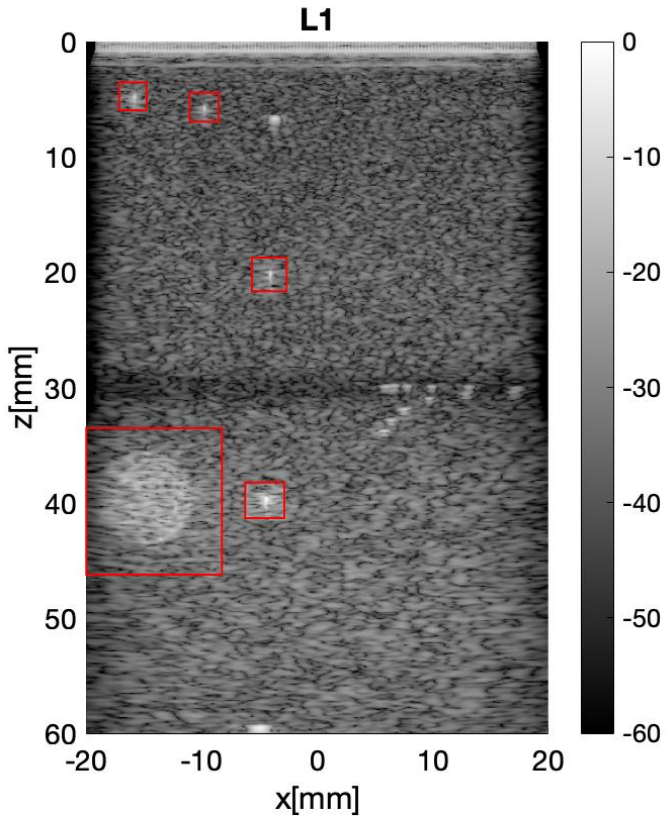

Figure 2.14: Hybrid image after L1 merging.

2.4.3 Dynamic-Range-Based (DR) Merging

In the third method, the merging process aims to equalize the dynamic range (DR) within a given ROI before after patch replacement. We have

$$DR_{NA} = max_i(|b_i{}^{NA}|) - min_i(|b_i{}^{NA}|) \tag{2.7}$$

$$DR_{MV} = max_i(|b_i{}^{MV}|) - min_i(|b_i{}^{MV}|), \tag{2.8}$$

where DR_{NA} is the dynamic range of the NA-DAS pixels, DR_{MV} is the dynamic range of the MV-DAS pixels, $max_i(|b_i|)$ is the maximum absolute value of all elements within the patch, and $min_i(|b_i|)$ is the minimum absolute value.

The corresponding scaling factor is given by

$$S_{DR} = DR_{NA}/DR_{MV}. \tag{2.9}$$

This factor is used to adjust the intensity of the MV-DAS pixels to the dynamic range of the NA-DAS pixels within the same ROI.

After this normalization step, the enhanced regions replace the target regions in the baseline image to complete the merging process. Fig. 2.15 demonstrates the effect of applying DR merging to the previous image example shown in Fig. 2.12.

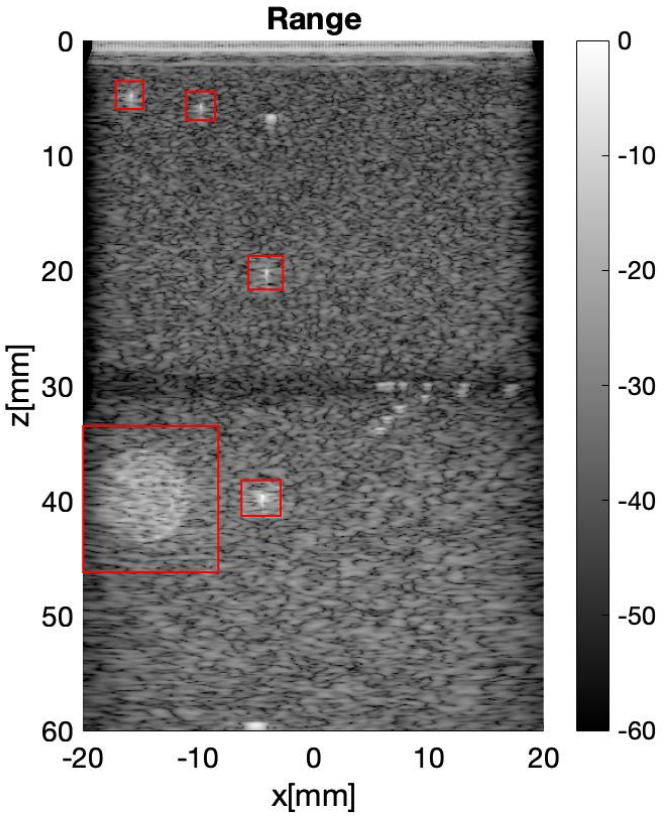

Figure 2.15: Hybrid image after DR merging.

2.4.4 Summary

Using the L2, L1, and DR merging techniques produces visually appealing results compared to the direct patch substitution. All techniques aim to achieve smooth data integration when replacing the enhanced regions with the target regions in a non-adaptive baseline image.

The L2 method uses the sum of the squared absolute values of ROI pixels to normalize the energy of the enhanced regions, thus equalizing the patch energy before and after replacement. The L1 method uses the sum of the absolute values of ROI pixels to normalize the intensity of the enhanced regions, thus equalizing the average intensity within each ROI patch before and after replacement. The DR method uses the dynamic range of ROI pixels to equalize the patch dynamic range before and after replacement.

Fig. 2.16 provides a side-by-side illustration of applying these three merging methods. As one can see, all of them produce visually similar results. In the sequel, we use the DR method due to its relatively low computational cost.

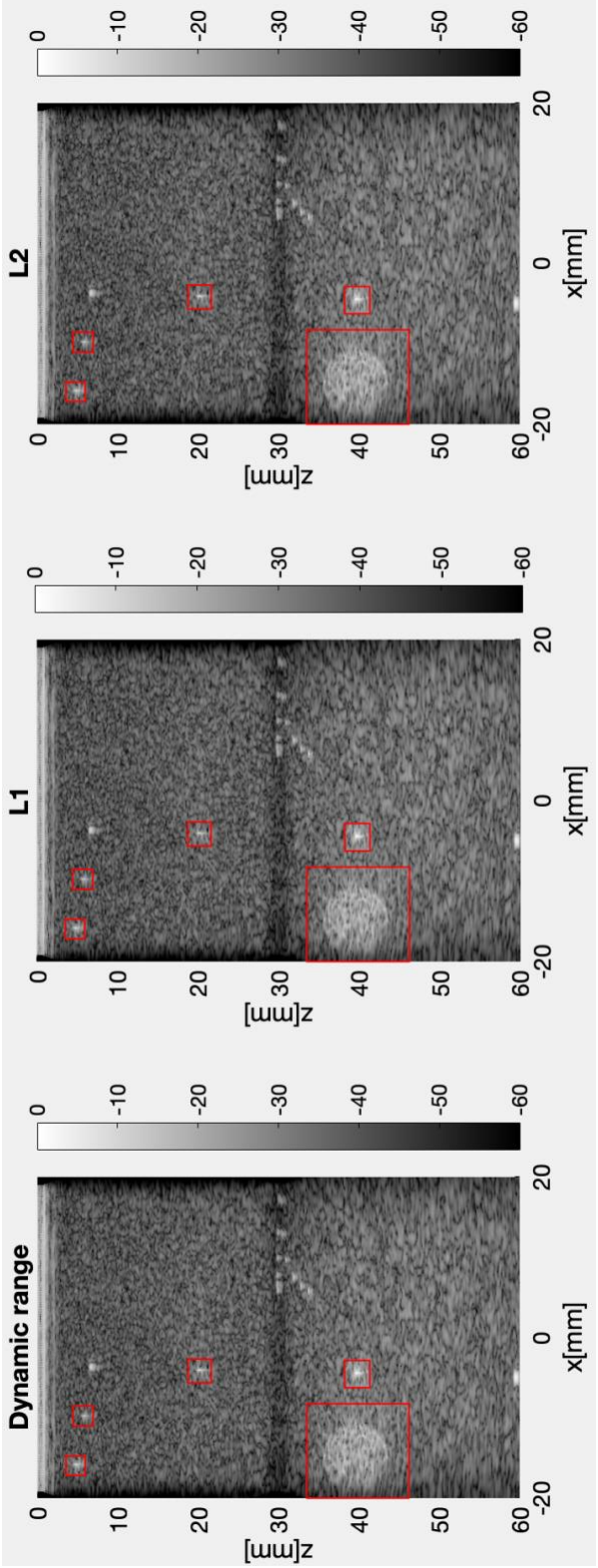

Figure 2.16: Comparison of three merging methods. From top to bottom: L2 merging, L1 merging, DR merging.

Chapter 3

Evaluation Results

We evaluate our proposed method on four datasets obtained from the USTB [1,11]. In this section we compare the NA-DAS, MV-DAS, and hybrid images, including the cross-sections of several detected ROIs. In two cases, we also provide the full width at half-maximum (FWHM) and contrast ratio (CR) values to quantify the resolution and contrast changes, respectively. Additionally, we report the execution runtimes to assess the computational cost.

3.1 Case 1 (Focused Imaging)

Case 1 (https://www.ustb.no/ustb-datasets/) is a focused imaging dataset of a hyperechoic cyst and point scatterers, recorded by an Alpinion scanner using an L3-8 probe on a CIRS phantom [11]. The acquired data contained 256 scan lines (3474 samples each), captured at a sampling frequency of 40 MHz. The L3-8 probe used 64 active elements (out of 128 total) during imaging. The sound speed was assumed to be equal to 1540 m/s, and the corresponding wavelength was 0.2567 mm. Fig. 3.1 shows the beamformed images for the following three scenarios: NA-DAS (all-pixel non-adaptive), MV-DAS (all-pixel adaptive), and hybrid (ROI-pixel adaptive). The size of each image is 601-by-401 pixels.

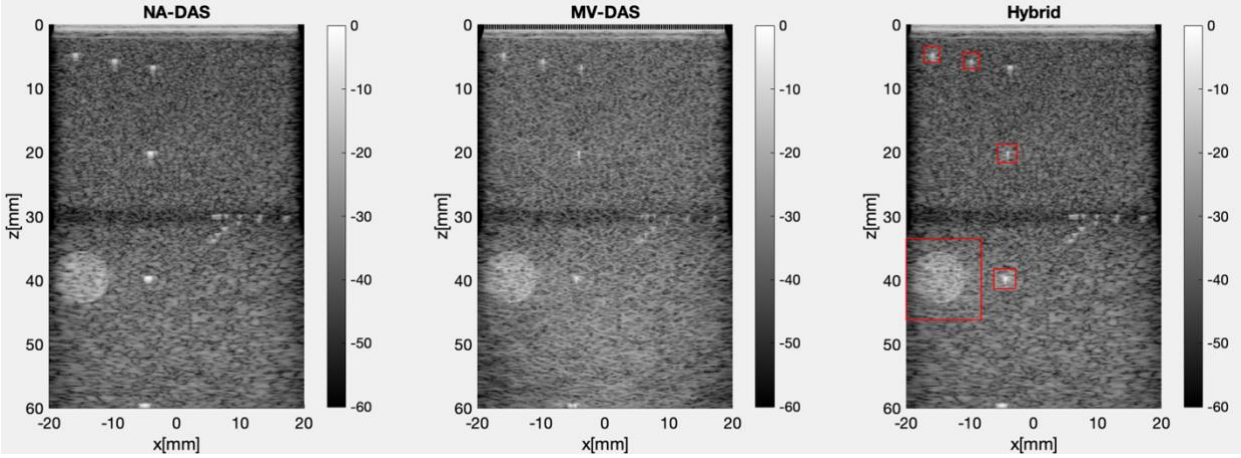

Figure 3.1: Case 1 beamforming results. From left to right: NA-DAS image, MV-DAS image, Hybrid image.

The hybrid image in Fig. 3.1 shows the bounding boxes where MV-DAS beamforming was applied. These bounding boxes were generated by our ROI detection method. It should be mentioned that during BTB object detection we set the minimum area threshold to zero in order to capture bright point targets for quantitative FWHM evaluation. Next, we show two lateral (horizontal) and two axial (vertical) cross-section plots to illustrate the effect of hybrid beamforming.

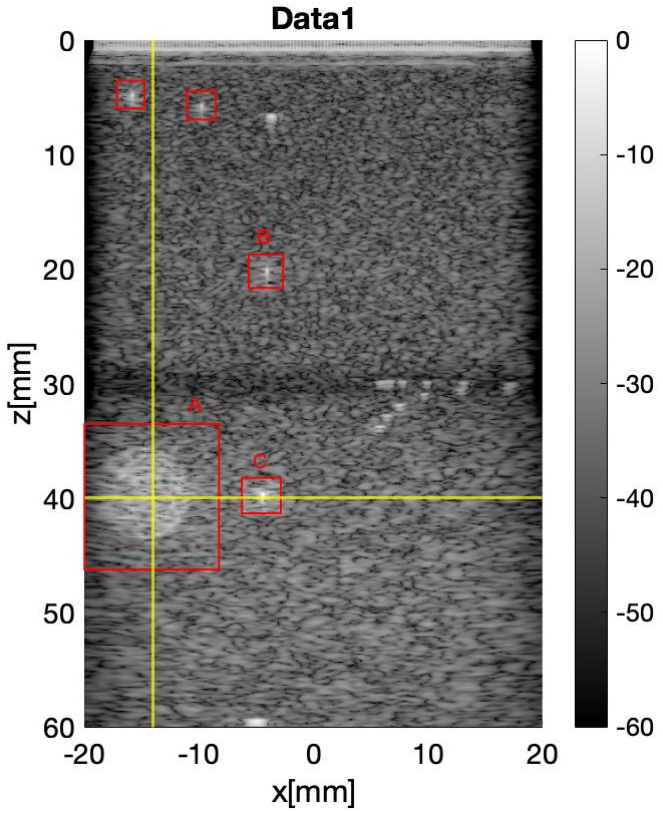

Figure 3.2: Horizontal and vertical cross-sections at midpoint of bounding box A.

The horizontal and vertical lines in Fig. 3.2 indicate the respective lateral and axial coordinates ($z = 40\ mm, x = -14\ mm$) of the two cross-sections through the midpoint of the bounding box A. The horizontal and vertical cross-section plots are shown in Fig. 3.3 and Fig. 3.4. The blue, red, and yellow curves correspond to the NA-DAS image, the MV-DAS image, and the hybrid image. Note that the horizontal cross-section also passes through the point target inside the bounding box C (see Fig. 3.2). Since adaptive beamforming improves resolution, we should be able to see a sharper peak in that target's location in the MV-DAS and hybrid data plots.

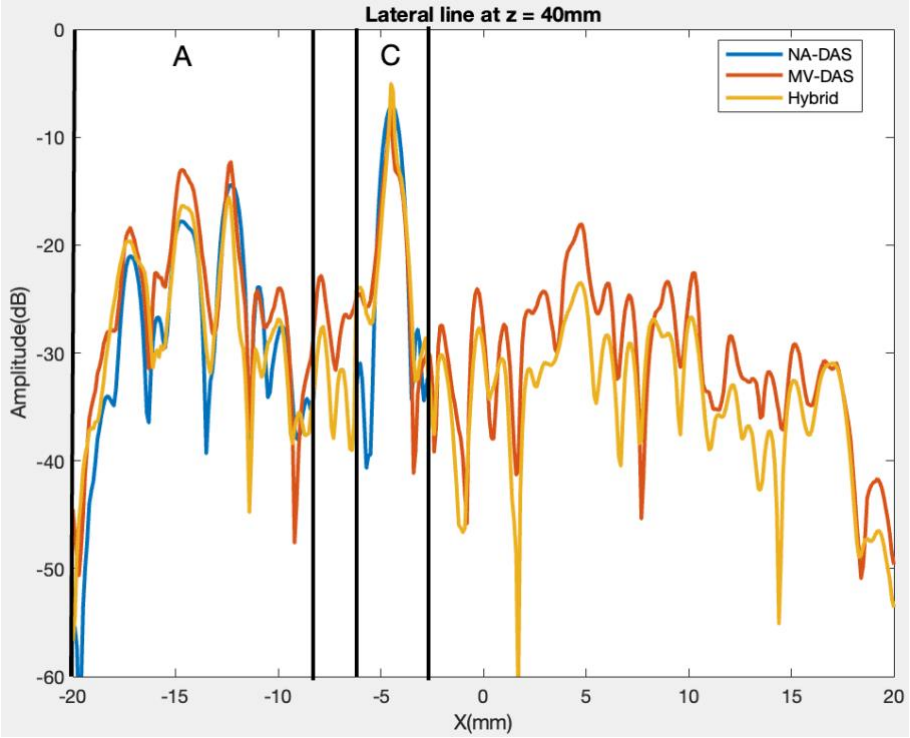

Figure 3.3: Horizontal cross-section comparison (Case 1, bounding box A).

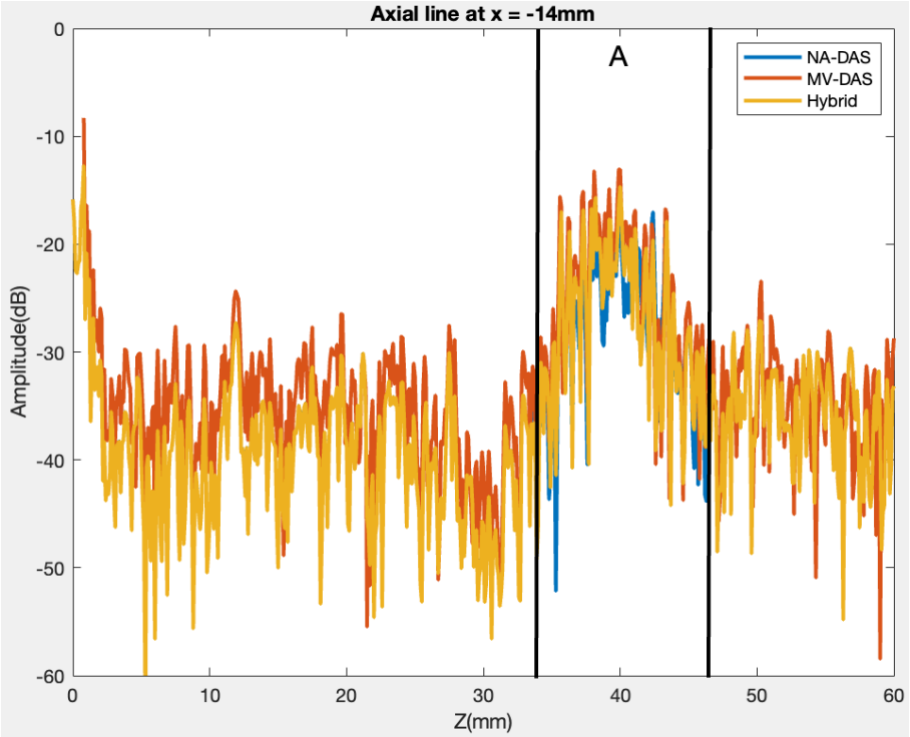

Figure 3.4: Vertical cross-section comparison (Case 1, bounding box A).

As one can see in Fig. 3.3 and Fig. 3.4, the NA-DAS and hybrid data values match exactly outside the bounding box boundaries. However, inside the ROI (i.e., within sections A and C in Fig. 3.3 and within section A in Fig. 3.4), the MV-DAS and hybrid data values may be different because of intensity scaling (i.e., DR merging) performed during ROI patch replacement. Inside section A in both figures, the hybrid data values tend to be larger than the NA-DAS ones, which suggests a slightly brighter appearance of a cyst target. Inside section C in Fig. 3.3, the peak curve of the hybrid data appears narrower compared to that of the NA-DAS data, which suggests better lateral resolution.

To quantify resolution improvements, we measure the FWHM of the peak curve in section C as shown in Fig. 3.5. The FWHM value for the NA-DAS curve is 0.87 mm, while the FWHM values for the MV-DAS and hybrid curves are significantly better, equal to 0.20 mm and 0.25 mm, respectively. These results clearly demonstrate that MV-DAS and hybrid beamforming achieve higher lateral resolution compared to NA-DAS beamforming.

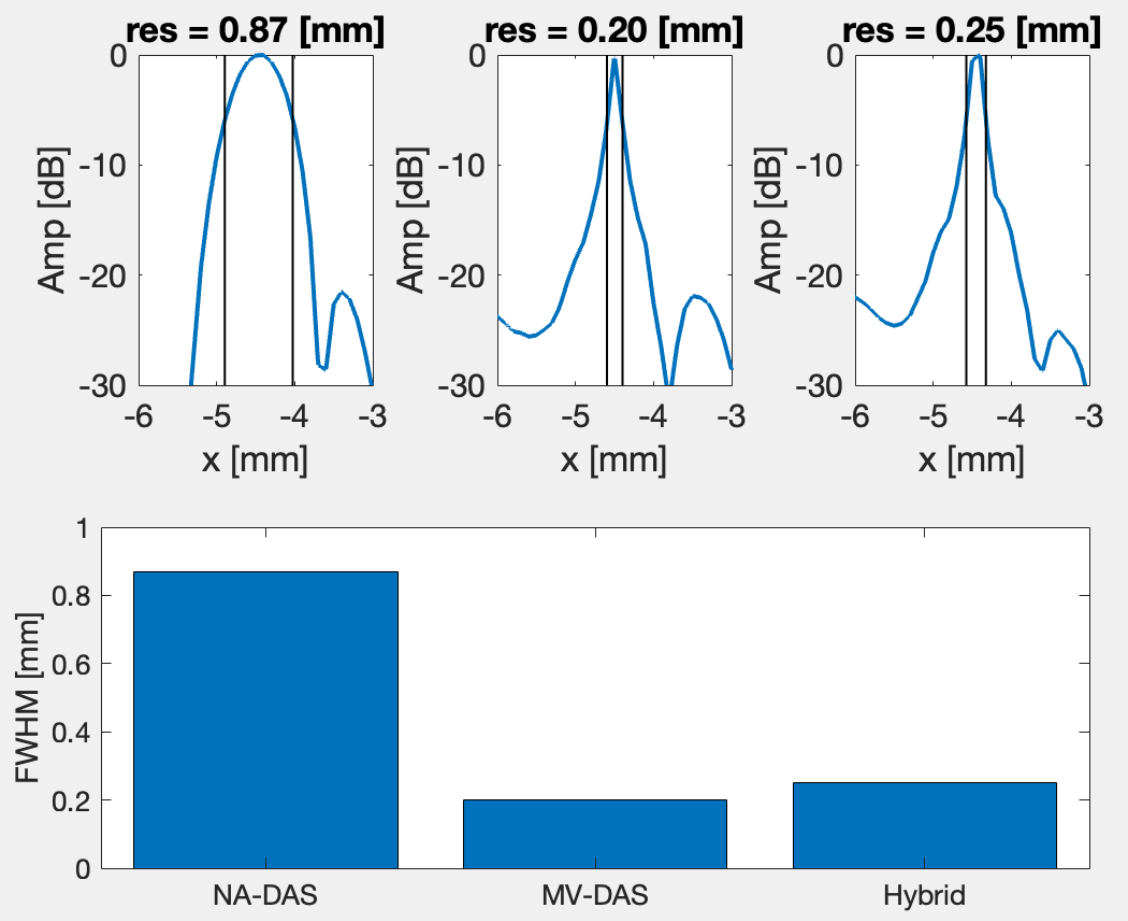

Figure 3.5: Lateral FWHM comparison (Case 1, bounding box C).

Fig. 3.6 shows another pair of cross-sections through the midpoint of the bounding box B ($z = 20\,mm, x = -5\,mm$). The corresponding horizontal and vertical cross-section plots are shown in Fig. 3.7 and Fig. 3.8.

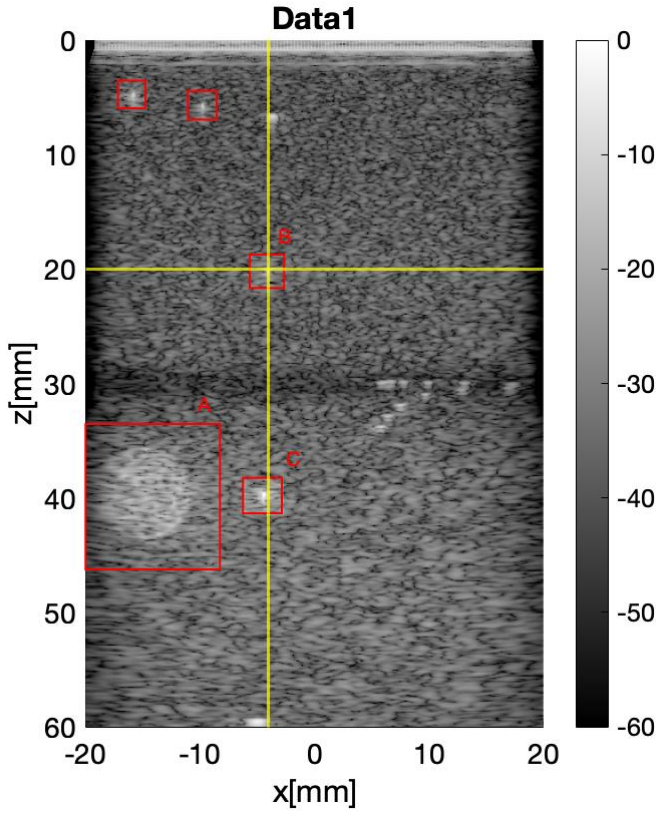

Figure 3.6: Horizontal and vertical cross-sections at midpoint of bounding box B.

As expected, Fig. 3.7 shows sharper peak curves formed by the MV-DAS and hybrid data (compared to the NA-DAS data), which suggests better lateral resolution within section B. However, Fig. 3.8 shows that the axial widths of the three peak curves under consideration do not differ significantly. These observations are confirmed in Fig. 3.9 presenting the FWHM measurements for section B. The lateral FWHM values for the MV-DAS and hybrid curves (0.17 mm and 0.10 mm) are substantially smaller compared to the NA-DAS data (0.66 mm). On the other hand, the axial FWHM values are relatively close to one another for the NA-DAS, MV-DAS, and hybrid curves (ranging between 0.44 mm and 0.39 mm). These results indicate that adaptive beamforming has a much greater impact on the lateral resolution than axial.

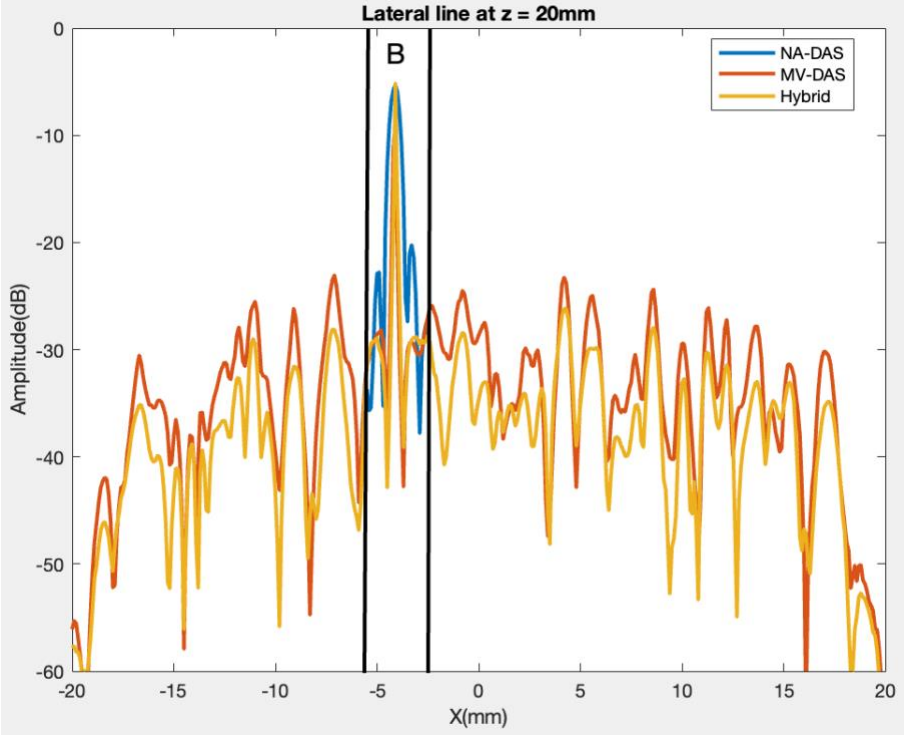

Figure 3.7: Horizontal cross-section comparison (Case 1, bounding box B).

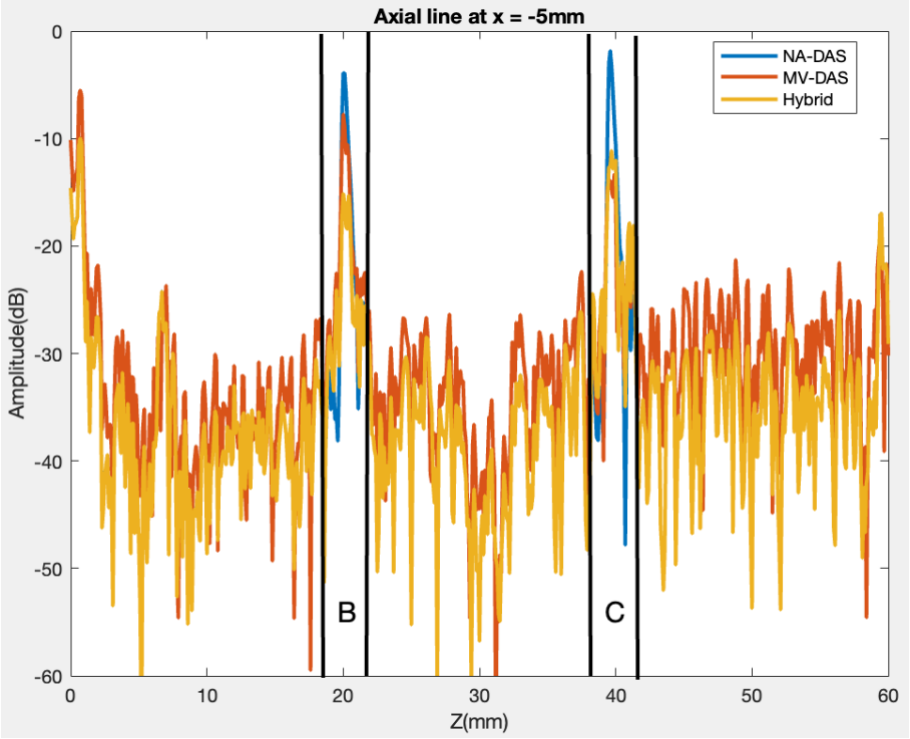

Figure 3.8: Vertical cross-section comparison (Case 1, bounding box B).

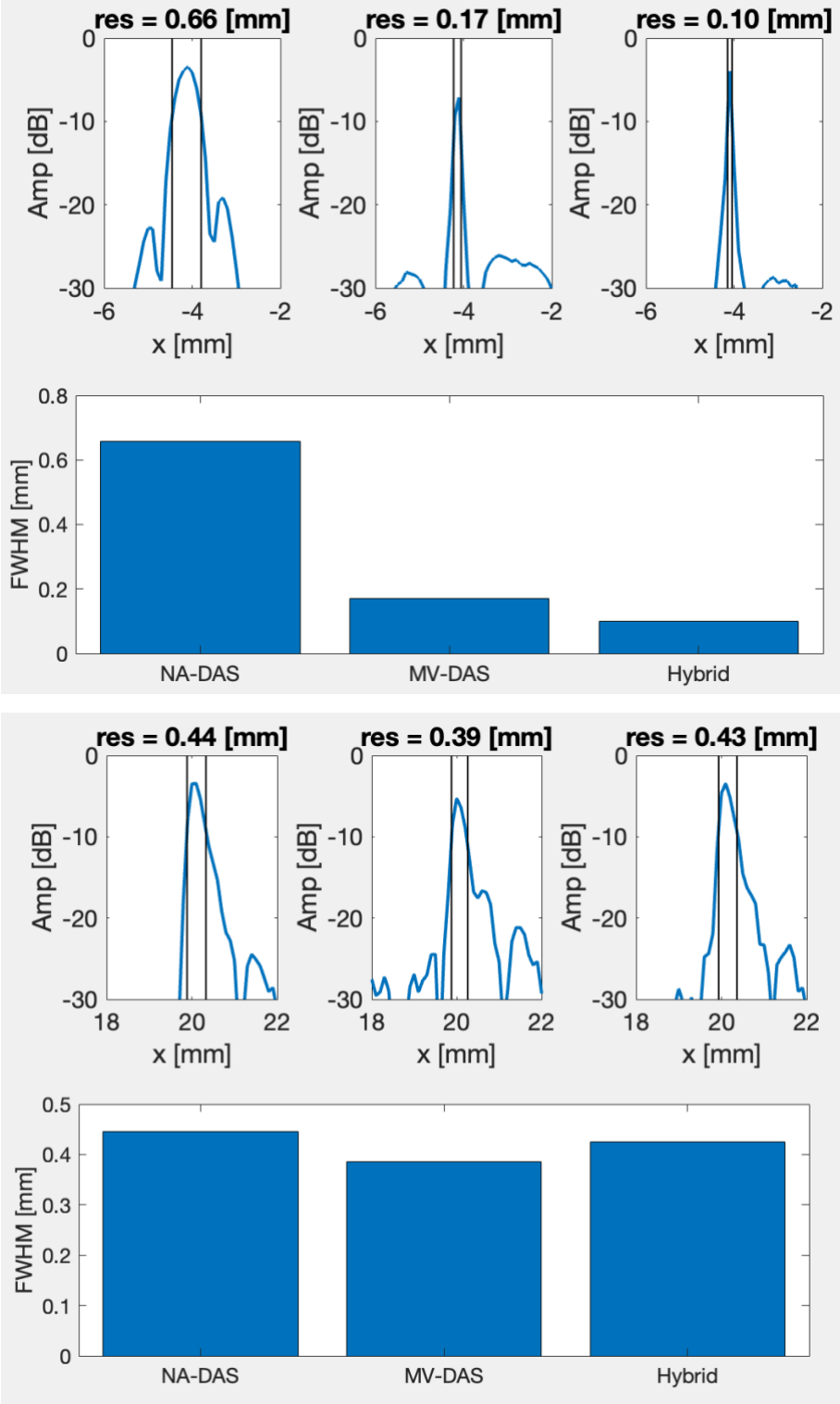

Figure 3.9: From top to bottom: Lateral and axial FWHM comparisons (Case 1, bounding box B).

Table 3.1: Runtime comparison in Case 1

Beamforming Method		**Run Time (s)**
Fully NA-DAS Beamforming		52.2
Fully MV-DAS Beamforming		270.8
Hybrid Beamforming	NA-DAS Beamforming	52.2
	ROI Detection	1.4
	MV-DAS Beamforming	84.1
	Merging	0.4

To assess the computational cost associated with our hybrid beamforming method, Table 3.1 shows the execution runtimes for the three scenarios under consideration. These results were obtained on a computer with the following specifications: USTB v2.3, MATLAB R2022a, macOS 14.5, CPU Apple M1 8-core processor, 3.2-GHz clock rate, 8-GB RAM. The running time of fully NA-DAS beamforming is 52.2 s, which is about five times faster than 270.8 s of fully adaptive beamforming. The proposed hybrid method's runtime is divided into four steps: NA-DAS beamforming, ROI detection, MV-DAS beamforming, and merging. The total running time of hybrid beamforming is 138.1 s, which is approximately twice as fast as fully adaptive beamforming. It should be noted that the computational overhead of ROI detection and merging is only 1.3% (1.8 s) of the overall execution runtime.

In conclusion, the results of Case 1 indicate that the hybrid image has significantly better lateral resolution within the ROIs than the NA-DAS image, as demonstrated by the FWHM measurements. Furthermore, hybrid beamforming runs 2.0 times faster than the fully adaptive method, as it applies MV-DAS beamforming only to pixels within detected ROIs.

3.2 Case 2 (Plane Wave Imaging)

Case 2 (https://www.ustb.no/ustb-datasets/) is a coherent plane wave compounding (CPWC) dataset acquired on a CIRS phantom with a Verasonics research scanner and an L11-4v probe for the PICMUS challenge [43]. The probe had 128 elements, all active during imaging. The sampling frequency was 20.832 MHz, and the plane wave (PW) center frequency was 5.208 MHz. Each raw data frame consisted of 3328 samples across 128 channels. There were 75 plane waves in total, and the corresponding 75 beamformed data frames were compounded to form the final CPWC image. Fig. 3.10 shows these images obtained by the NA-DAS, MV-DAS, and hybrid beamforming methods. The size of each image is 601-by-401 pixels.

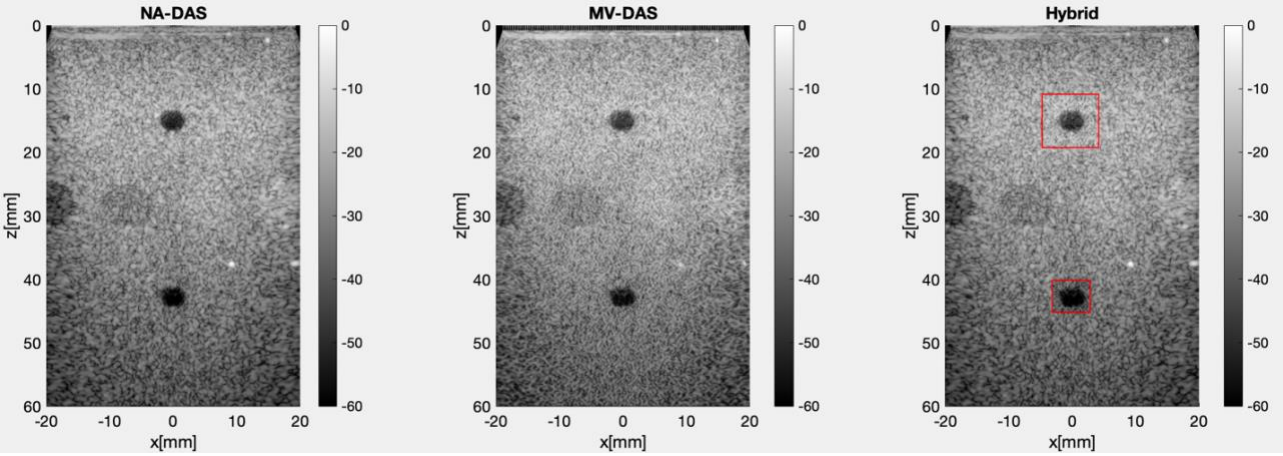

Figure 3.10: Case 2 beamforming results. From left to right: NA-DAS image, MV-DAS image, Hybrid image.

The detected ROI bounding boxes are shown in red in Fig. 3.10. We have used the default threshold settings for the minimum and maximum ROI area (see Chapter 2). Next, we examine the lateral and axial cross-sections through the midpoint of the bounding box A ($z = 15\,mm$, $x = 0\,mm$), as illustrated in Fig. 3.11.

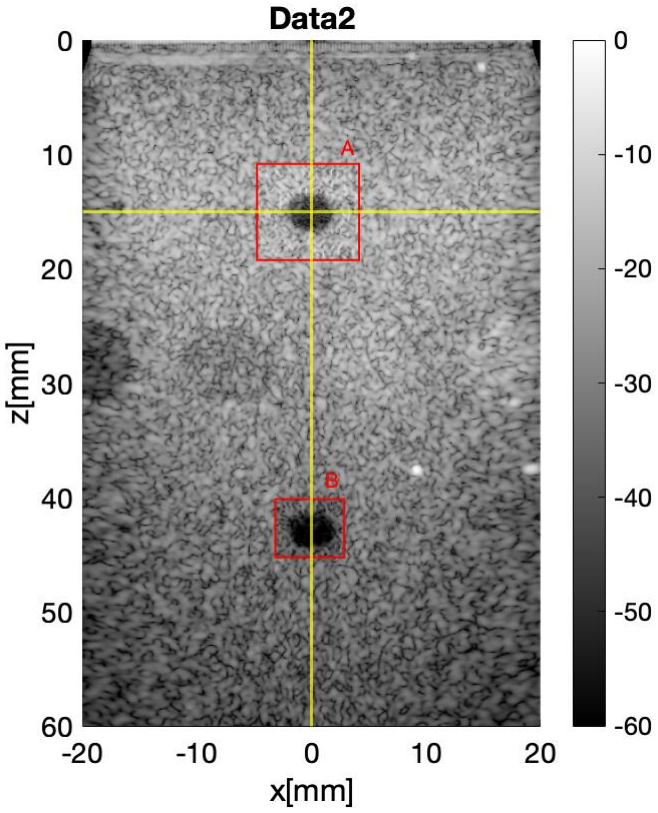

Figure 3.11: Horizontal and vertical cross-sections at midpoint of bounding box A.

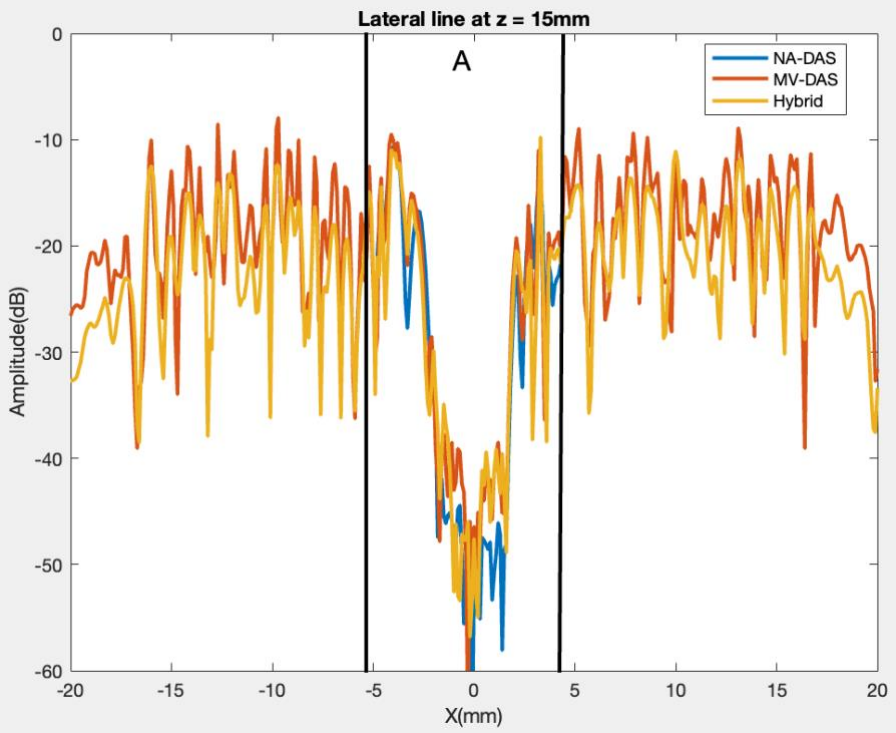

Figure 3.12: Horizontal cross-section comparison (Case 2, bounding box A).

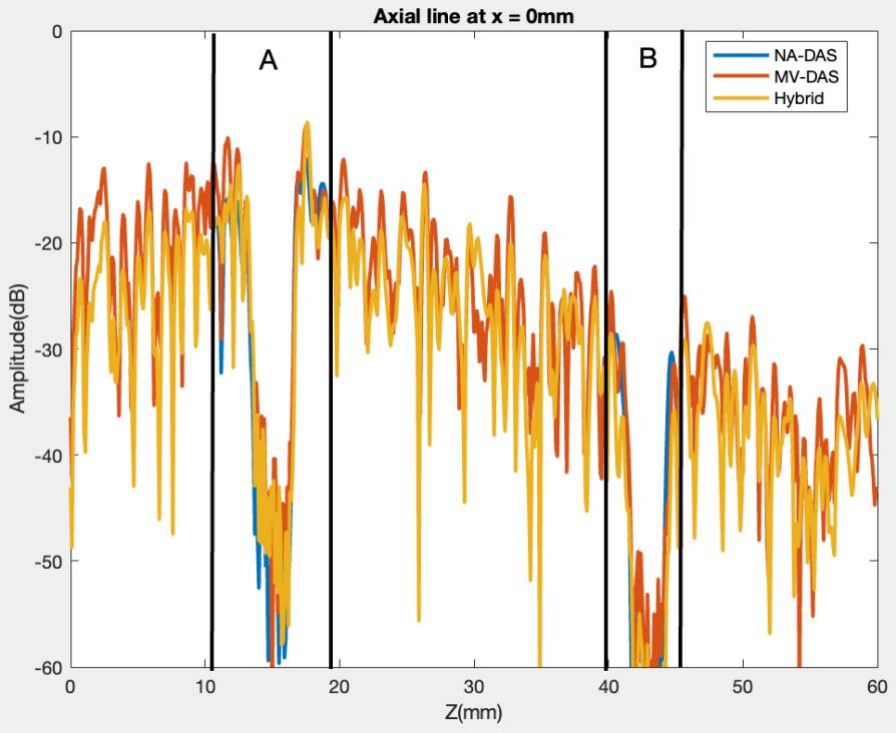

Figure 3.13: Vertical cross-section comparison (Case 2, bounding box A).

Fig. 3.12 and Fig. 3.13 show horizontal and vertical cross-section plots of the NA-DAS, MV-DAS, and hybrid image data. As one can see, the NA-DAS curves within the A section reach slightly lower values compared to the MV-DAS and hybrid ones, which suggests that the cyst pixels are slightly darker in the NA-DAS case. This is confirmed in Fig. 3.14 depicting the contrast ratio (CR) measurement for the two areas delineated by the red circle (cyst area) and the concentric yellow circle pair (background area). The NA-DAS method yields the highest CR of 27.18, followed by the MV-DAS and hybrid methods with the CR values of 24.71 and 24.25, respectively. While the hybrid method enhances resolution within the ROI, it does not improve contrast when compared to the NA-DAS method.

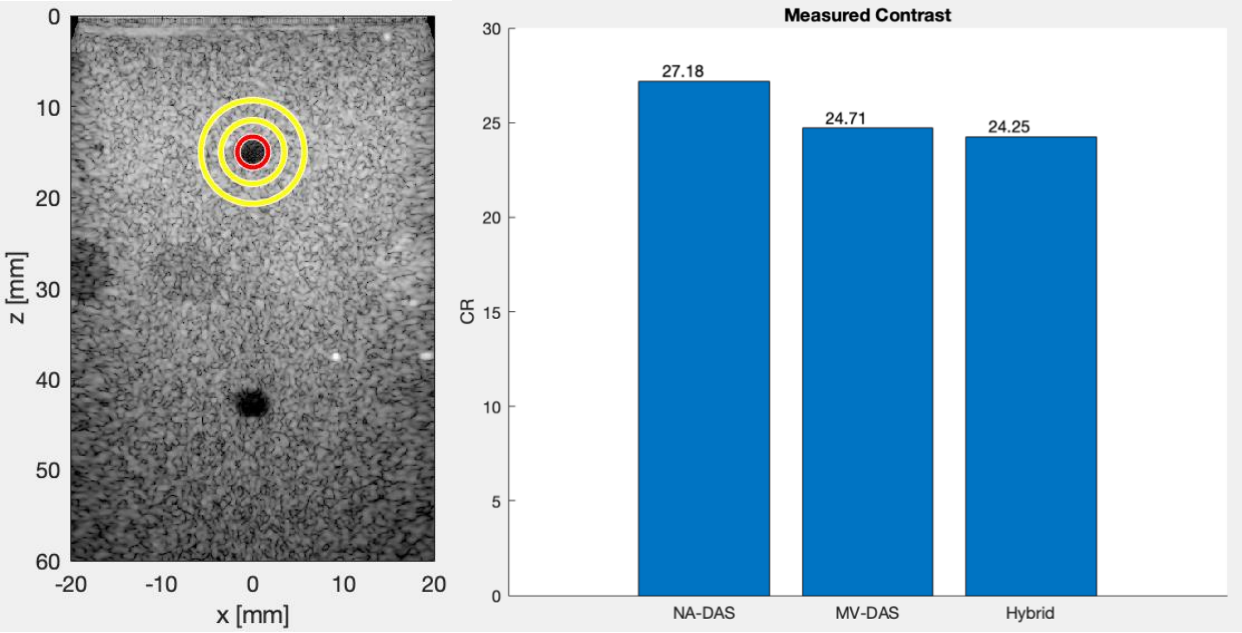

Figure 3.14: Contrast ratio comparison (Case 2, bounding box A).

A similar observation can be made for the bounding box B in Fig. 3.15, whose lateral and axial cross-section plots ($z = 43\,mm, x = 0\,mm$) are shown in Fig. 3.16 and Fig. 3.17. The contrast ratio measurements depicted in Fig. 3.18 indicate the hybrid method yields CR = 26.34, which is slightly higher than 25.15 of the NA-DAS method. While this is an improvement compared to the measurements shown in Fig. 3.14, the hybrid method is not significantly better than the NA-DAS method in terms of their respective CR values.

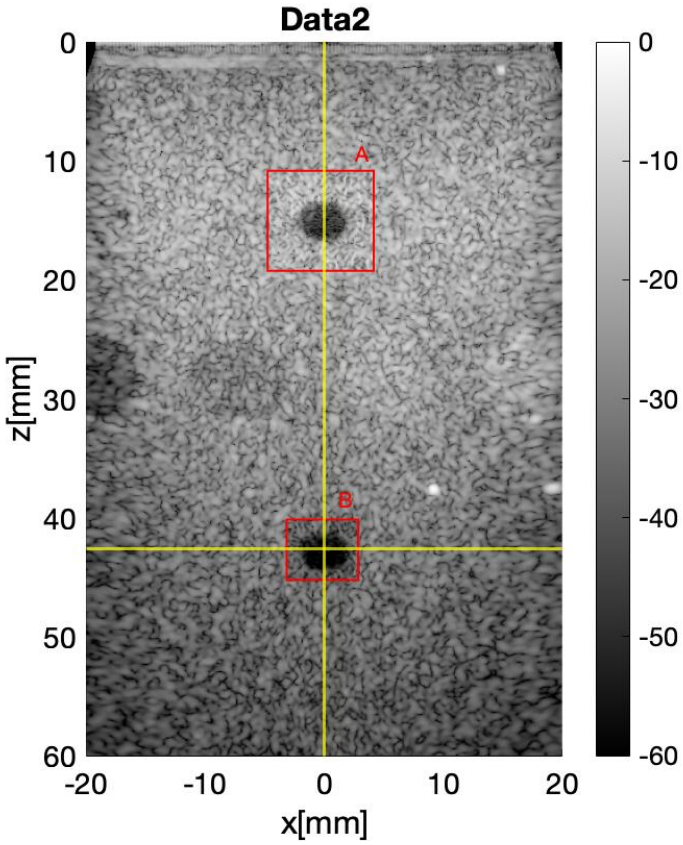

Figure 3.15: Horizontal and vertical cross-sections at midpoint of bounding box B.

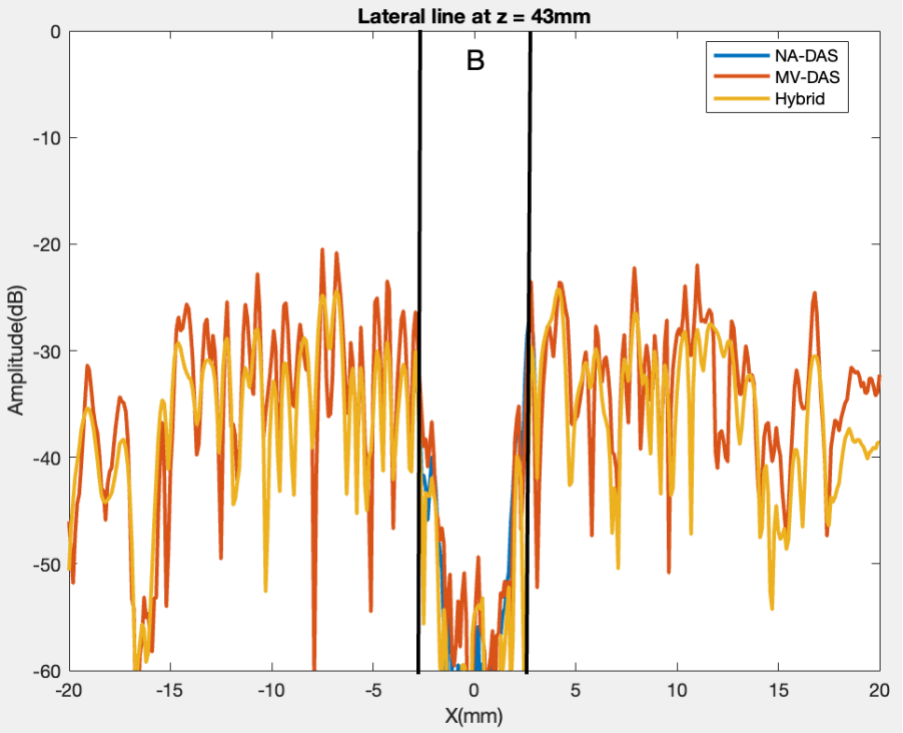

Figure 3.16: Horizontal cross-section comparison (Case 2, bounding box B).

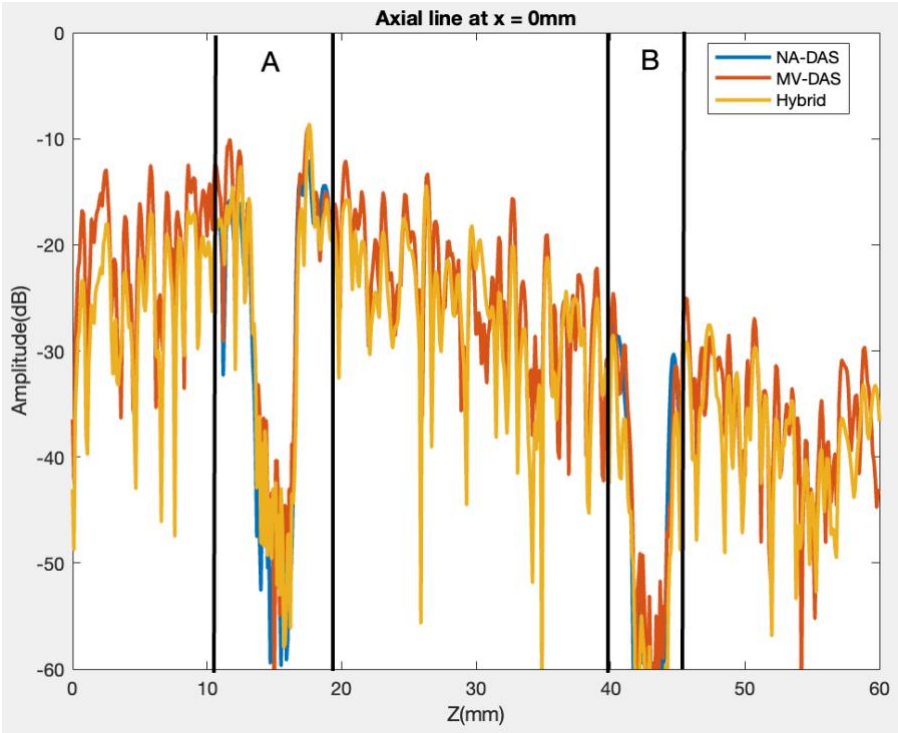

Figure 3.17: Vertical cross-section comparison (Case 2, bounding box B).

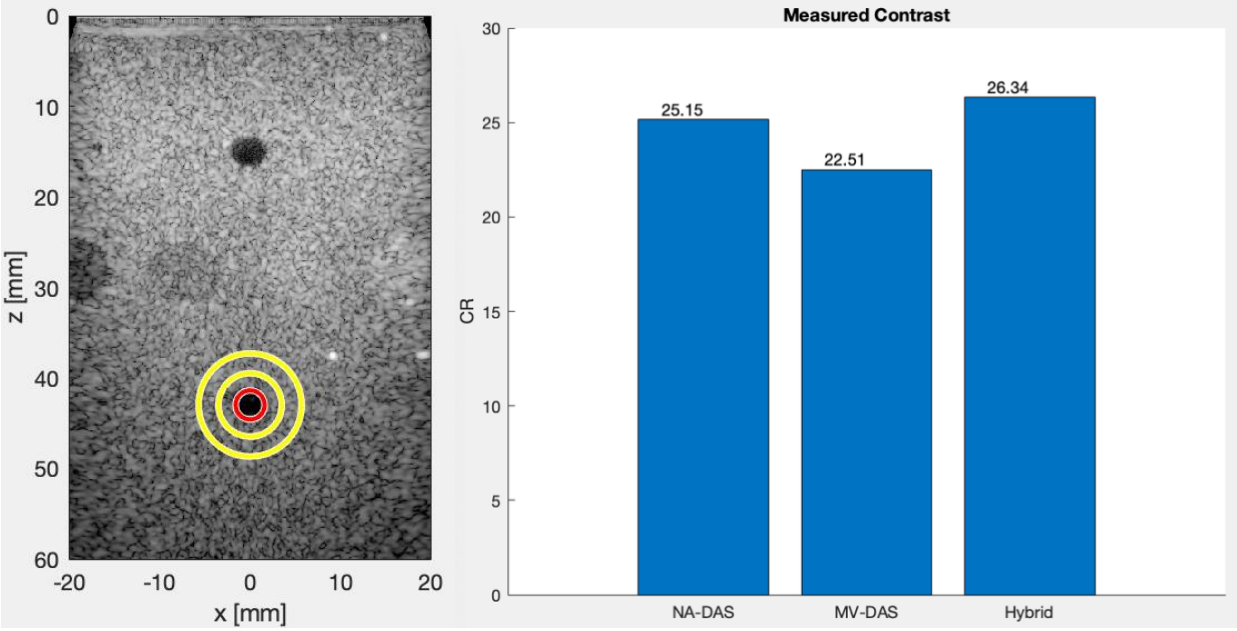

Figure 3.18: Contrast ratio comparison (Case 2, bounding box B).

Table 3.2: Runtime comparison in Case 2

Beamforming Method		**Run Time (s)**
Fully NA-DAS Beamforming		21.0
Fully MV-DAS Beamforming		239.0
Hybrid Beamforming	NA-DAS Beamforming	21.0
	ROI Detection	1.9
	MV-DAS Beamforming	18.6
	Merging	0.5

Table 3.2 shows the execution runtimes in Case 2 for each method under consideration. The running time of NA-DAS beamforming is 21.0 s, which is 11.4 times faster than 239.0 s of

MV-DAS beamforming when applied to all pixels. The running time for the proposed hybrid method has a total running time of 42.0 s, which is 5.7 times faster than fully adaptive beamforming.

Case 2 demonstrates that the hybrid method does not have a significant impact on the contrast of DTB regions (dark cysts in this example) compared to the NA-DAS method. This case illustrates an important limitation of adaptive beamforming: the latter does not necessarily result in superior image quality in terms of contrast-related measurements (unlike resolution-related measurements reported for Case 1).

3.3 Case 3 (Plane Wave Imaging)

Case 3 (https://www.ustb.no/ustb-datasets/) is another CPWC dataset. It contains the raw data for a hyperechoic cyst and point scatterers from a CIRS phantom, recorded by an Alpinion scanner with an L3-8 probe. The probe had 128 elements, all active during imaging. Each raw data frame consisted of 4352 samples across 128 channels, with a total of 21 plane waves used for coherent compounding. The sampling frequency was 40 MHz, and the PW wavelength was 0.2567 mm. Fig. 3.19 shows the CPWC images obtained by NA-DAS, MV-DAS, and hybrid beamforming. The size of each image is 601-by-401 pixels.

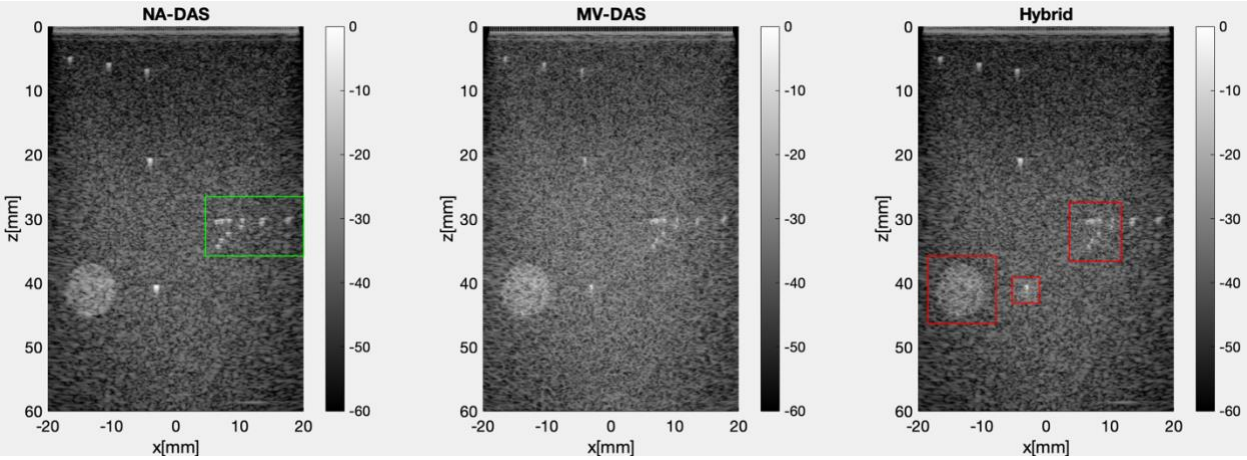

Figure 3.19: Case 3 beamforming results. From left to right: NA-DAS image, MV-DAS image, Hybrid image.

The red bounding boxes in Fig. 3.19 indicate the detected ROIs, whose pixels were beamformed adaptively by our hybrid method. The green bounding box symbolizes the zoomed-in section shown in Fig. 3.20 for visual comparison.

As one can see in Fig. 3.20, the MV-DAS image has much better lateral resolution compared to the NA-DAS image. The point targets appear sharper individually, and the speckled background is also less blurry in the MV-DAS image.

The hybrid image combines the results from both NA-DAS and MV-DAS beamforming. The ROI point targets are sharper, similar to the MV-DAS image, but their intensity is more consistent with the NA-DAS image. The pixels outside the ROI are identical to those of the NA-DAS image. This indicates that the hybrid image correctly applied adaptive beamforming to the selected ROI pixels, which improved resolution while keeping brightness levels relatively intact. However, the transition across the ROI boundary (near $x = 12\,mm$) is not visually seamless, which means that the merging step of the hybrid method needs further refinement. This issue will be addressed in the future work by exploring advanced image fusion techniques.

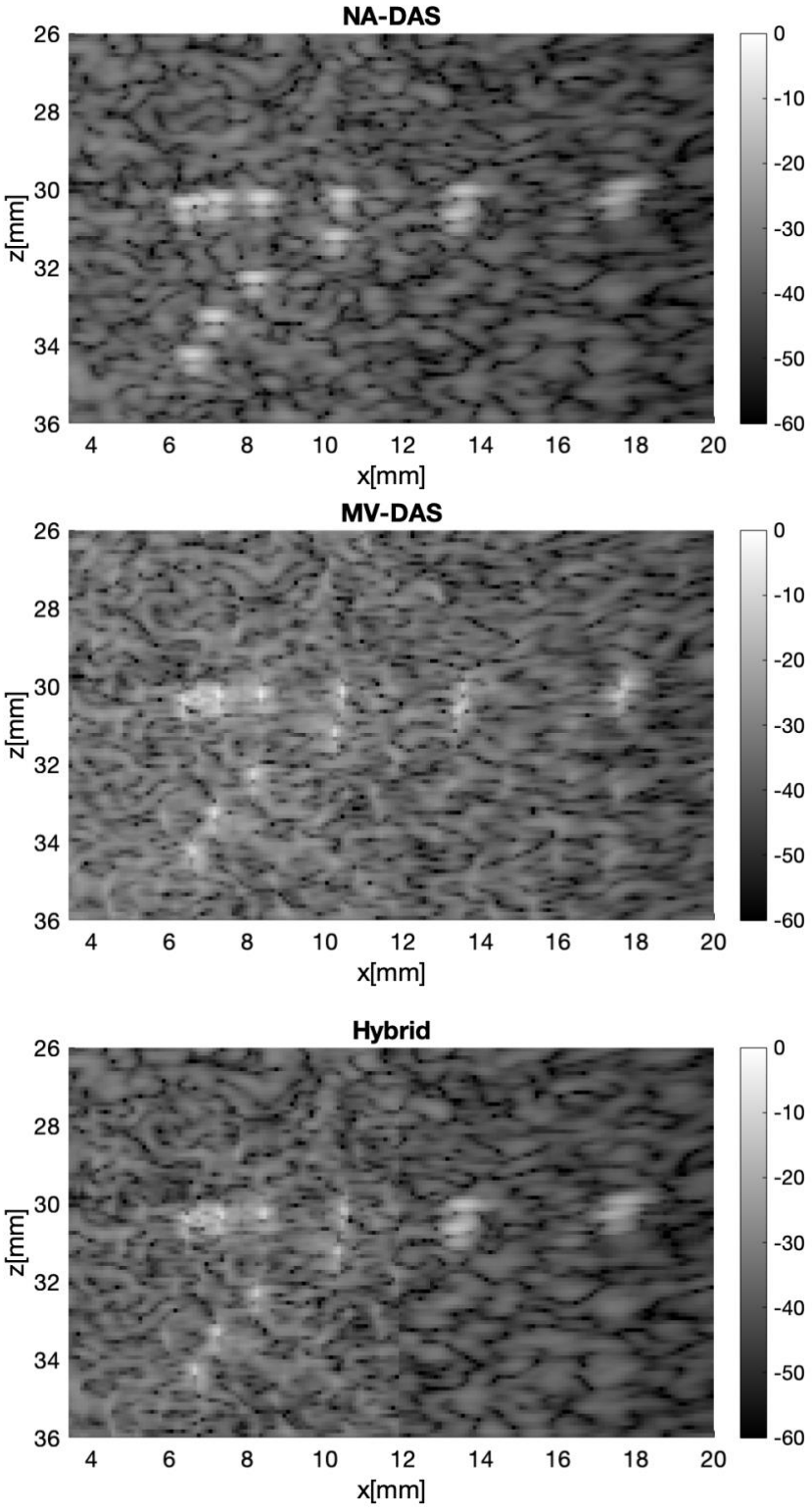

Figure 3.20: Zoom-in section comparison. From top to bottom: NA-DAS image, MV-DAS image, Hybrid image.

Table 3.3. Runtime comparison in Case 3

Beamforming Method		**Run Time (s)**
Fully NA-DAS Beamforming		7.8
Fully MV-DAS Beamforming		296.0
Hybrid Beamforming	NA-DAS Beamforming	7.8
	ROI Detection	2.4
	MV-DAS Beamforming	31.0
	Merging	0.7

Table 3.3 shows the execution runtimes for Case 3. The running time of fully non-adaptive (NA-DAS) beamforming is 7.8 s, which is 38.0 times faster than 296.0 s of fully adaptive (MV-DAS) beamforming. The hybrid method has a total running time of 41.9 s, which is 7.1 times faster than that of fully adaptive beamforming.

The results of Case 3 reveal that the ROI pixels of the hybrid image appear sharper due to increased resolution, yet their brightness levels are consistent with those of the NA-DAS image. Furthermore, the hybrid method is approximately seven times faster than the MV-DAS beamforming. However, the merging step needs to be improved to make the transition across the ROI boundaries visually seamless.

3.4 Case 4 (Focused Imaging)

Case 4 (https://www.ustb.no/ustb-datasets/) is another focused imaging dataset acquired by an Alpinion scanner with a L3-8 probe on a CIRS phantom [11]. The probe had 128 elements, with 64 elements active during imaging. Each scan line consisted of 3474 samples across 128 channels, with a total of 256 scan lines forming a single image frame. The sampling frequency was 40 MHz, and the transmitted beam wavelength was 0.2567 mm. The images produced by the NA-DAS, MV-DAS, and hybrid methods are shown in Fig. 3.21. The size of each image is 601-by-401 pixels.

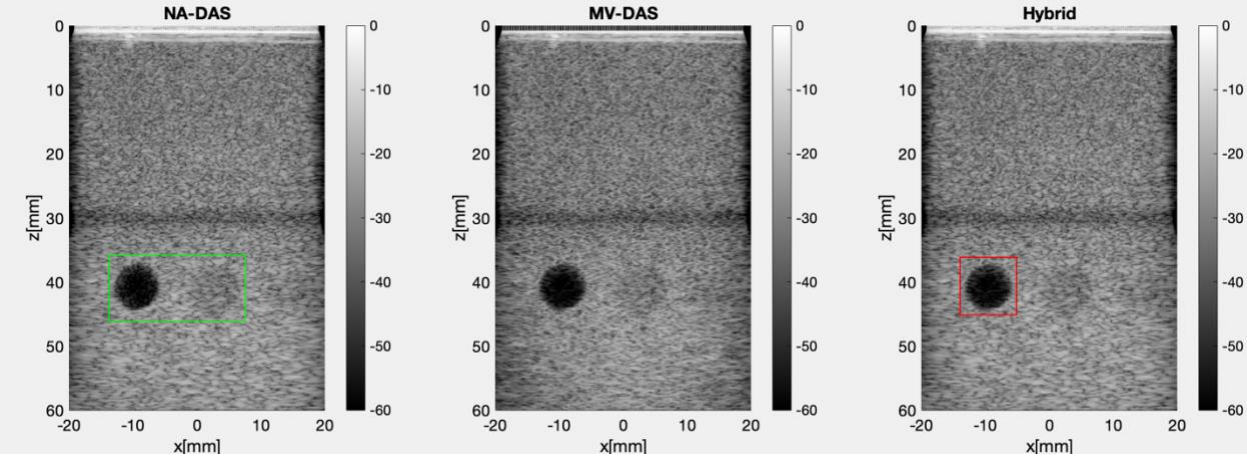

Figure 3.21: Case 4 beamforming results. From left to right: NA-DAS image, MV-DAS image, Hybrid image.

The red bounding box in Fig. 3.21 depicts the detected ROI (using the default settings described in Chapter 2), while the green bounding box delineates the zoom-in section of the images, used for visual comparison. The corresponding image patches are shown in Fig. 3.22.

As one can see, the visual appearance of the DTB object (dark cyst) is slightly better in the MV-DAS image compared to the NA-DAS image: more pixels are dark, and the cyst shape is more circular. The hybrid image is similar to the MV-DAS image in terms of the cyst shape, but many of the cyst pixels are not as dark, which can be attributed to the limitation of the merging step. On the other hand, the transition across the ROI boundary (near $x = -5\,mm$) is not visually noticeable, which indicates that merging was relatively successful. Overall, image enhancements offered by the hybrid method over NA-DAS beamforming do not appear to be significant in this example.

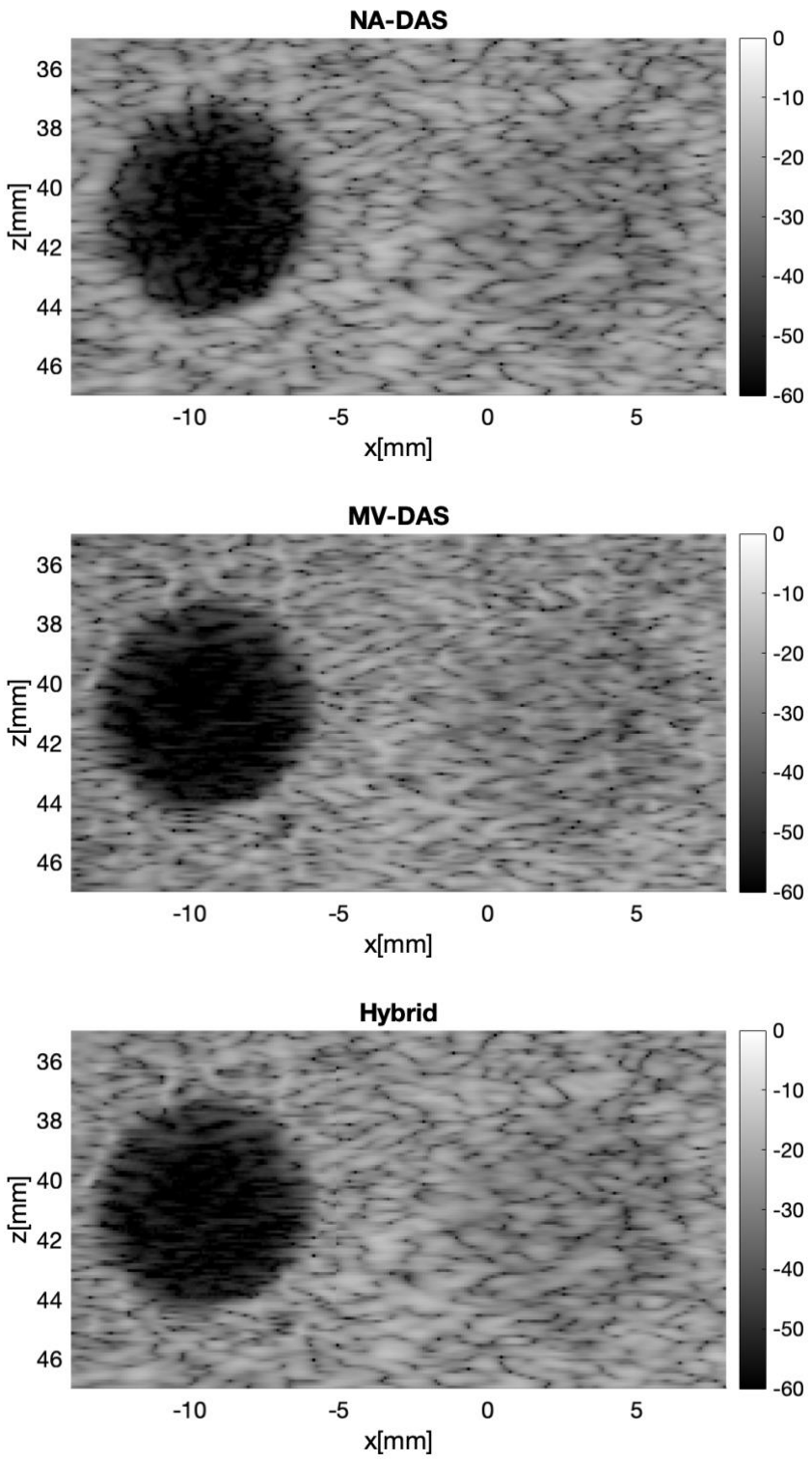

Figure 3.22: Zoom-in section comparison. From top to bottom: NA-DAS image, MV-DAS image, Hybrid image.

Table 3.4: Runtime comparison in Case 4

Beamforming Method		**Run Time (s)**
Fully NA-DAS Beamforming		50.7
Fully MV-DAS Beamforming		285.1
Hybrid Beamforming	NA-DAS Beamforming	50.7
	ROI Detection	1.8
	MV-DAS Beamforming	26.8
	Merging	0.5

The execution runtimes of the three methods under consideration are displayed in Table 3.4. The running time of fully NA-DAS beamforming is 5.6 times faster than that of fully MV-DAS beamforming (50.7 s compared to 285.1 s). The hybrid method has a total running time of 79.8 s, which is 3.6 times faster than fully adaptive beamforming.

The results of Case 4 indicate that the hybrid image is slightly better than the NA-DAS image in terms of the visual appearance of the DTB cyst object (more circular shape), but it does not match the quality of the MV-DAS image (fewer dark pixels) because of merging limitations. However, the hybrid method runs nearly four times faster than the MV-DAS method, which demonstrates its practical value.

3.5 Summary

Table 3.5: Comparative Summary

	Case 1	Case 2	Case 3	Case 4
Fully NA-DAS Beamforming	52.2 s	21.0 s	7.8 s	50.7 s
Fully MV-DAS Beamforming	270.8 s	239.0 s	296.0 s	285.1 s
Hybrid Beamforming	138.1 s	42.0 s	41.9 s	79.8 s
Lateral Resolution	Significant Improvement (Fig. 3.5, 3.9)	N/A	Significant Improvement (Fig. 3.20)	N/A
Axial Resolution	Insignificant Improvement (Fig. 3.9)	N/A	Insignificant Improvement (Fig. 3.20)	N/A
Contrast	N/A	Inconclusive (Fig. 3.14, 3.18)	N/A	Insignificant Improvement (Fig. 3.22)

Table 3.5 shows the comparative summary of our evaluation results. One can see that the hybrid beamforming method is faster than fully adaptive MV-DAS beamforming across all cases. The benefits of using hybrid beamforming are demonstrated in Cases 1 and 3 that indicate significant improvements in lateral resolution compared to NA-DAS beamforming; however, axial resolution is not improved significantly. In Case 4, the contrast is slightly better in the hybrid case, due to the increased number of dark pixels within an anechoic cyst image section. In Case 2, however, the CR measurements are inconclusive: they are slightly better for the bottom cyst but slightly worse for the top cyst.

It is important to reiterate that the computational efficiency of our hybrid method arises from applying MV-DAS beamforming only within detected ROIs, as opposed to applying MV-DAS beamforming over all image pixels. While hybrid beamforming is obviously more expensive

than NA-DAS beamforming, it offers significantly better lateral resolution within ROIs. On the other hand, if the target image quality emphasizes axial resolution or contrast, the use of costly MV-DAS beamforming (either within ROIs, or over all pixels) is unlikely to yield significant improvements. Finally, it should be noted that the execution runtimes summarized in Table 3.5 are not compatible with real-time performance requirements, as these measurements were taken on a general-purpose laptop PC. Achieving real-time performance would require dedicated hardware support (e.g., GPU-based acceleration).

Chapter 4

Conclusion and Future Work

4.1 Conclusion

In this work, we have proposed a hybrid receive beamforming method that aims to improve ultrasound image reconstruction by balancing computing efficiency and image quality. Our strategy is to utilize non-adaptive (NA-DAS) beamforming to obtain a baseline image first, and then apply adaptive (MV-DAS) beamforming only within specific regions of interest (ROIs) found using brighter-than-background (BTB) and darker than-background (DTB) object detection (see Chapter 2). This hybrid method combines the benefits of both non-adaptive and adaptive beamforming techniques to produce selectively high-resolution images at a generally low computational cost.

The evaluation results from four experimental cases show that the hybrid approach achieves higher resolution with target regions than fully non-adaptive beamforming while significantly reducing its execution runtime compared to fully adaptive beamforming (see Chapter 3). For example, the lateral FWHM of two point targets in Case 1 was improved from 0.87 and 0.66 mm down to 0.25 and 0.10 mm, respectively. On the other hand, MV-DAS beamforming did not have a substantial impact on axial FWHM (measured in Case 1) or CR (measured in Case 2), which suggests that utilizing an expensive adaptive beamformer may not always be beneficial.

This work has many limitations that should be addressed in the future. The ROI detection method used here is fairly simple. It relies on image binarization, finding clusters, evolving active contours, and applying morphological filtering and area thresholds. Accurately detecting relevant

ROIs can be challenging and requires further study. Also, the merging step of our hybrid method, which replaces NA-DAS pixels with MV-DAS ones within a ROI, is currently based on pixel intensity normalization using a single scaling factor. It is worthwhile to explore more sophisticated techniques for pixel blending.

4.2 Future Work

Improving the ROI detection method is a priority. The goal is to investigate more advanced object detection algorithms, such as deep learning-based approaches. Convolutional neural networks (CNNs) are a technique that can dramatically enhance ROI detection accuracy and recall.

It may be possible to enhance ROI detection accuracy by fine-tuning pre-trained models such as ResNet [44], Faster R-CNN [45], YOLO [46], and SSD [47] using the ultrasound data. The procedure entails creating a diverse dataset, selecting appropriate CNN architectures, and implementing transfer learning or end-to-end training. Multi-scale detection [48], anchor boxes [49], and non-maximum suppression (NMS) [50] are important strategies for dealing with variable item sizes and eliminating redundant detections.

Another focus could be on more advanced merging techniques. The goal is to investigate adaptive merging algorithms that dynamically adjust merging parameters based on the properties of the detected regions. This includes using machine learning and image fusion methods to enhance the merging process. Any improvements to intensity-based, energy-based, and/or gradient-based merging approaches will need to ensure seamless blending of MV-DAS and NA-DAS pixels across ROI boundaries.

Finally, we also suggesting investigating additional resolution-enhancing and contrast-enhancing techniques, such as single-image super-resolution (SISR) [51] and contrast-limited

adaptive histogram equalization (CLAHE) [52], to improve the overall quality of ultrasound images. Using these strategies can help highlight finer details and increase the diagnostic value of the images, particularly within ROIs. By balancing these enhancements with computational efficiency, one may be able to improve image quality without significantly extending processing time.

Bibliography

[1] O. M. H. Rindal, "Software Beamforming in Medical Ultrasound Imaging - A Blessing and a Curse," Ph.D. dissertation, University of Oslo, 2020. https://www.duo.uio.no/handle/10852/73764.

[2] O. M. H. Rindal, A. Austeng, A. Fatemi, and A. Rodriguez-Molares, "The Effect of Dynamic Range Alterations in the Estimation of Contrast," *IEEE Transactions on Ultrasonics, Ferroelectrics, and Frequency Control*, vol. 66, no. 7, pp. 1198–1208, 2019, doi: 10.1109/TUFFC.2019.2911267.

[3] J.-F. Synnevag, A. Austeng, and S. Holm, "Benefits of Minimum-Variance Beamforming in Medical Ultrasound Imaging," *IEEE Transactions on Ultrasonics, Ferroelectrics, and Frequency Control*, vol. 56, no. 9, pp. 1868–1879, 2009, doi: 10.1109/TUFFC.2009.1263.

[4] O. M. H. Rindal, S. Aakhus, S. Holm, and A. Austeng, "Hypothesis of Improved Visualization of Microstructures in the Interventricular Septum with Ultrasound and Adaptive Beamforming," *Ultrasound in Medicine & Biology*, vol. 43, no. 10, pp. 2494–2499, 2017, doi: 10.1016/j.ultrasmedbio.2017.05.023.

[5] S. Eddins, "Use Imbinarize to Threshold Gray-scale Images," Steve on Image Processing with MATLAB, 2021. https://blogs.mathworks.com/steve/2021/06/17/use-imbinarize-to-threshold-gray-scale-images.

[6] R. C. Gonzalez, R. E. Woods, and S. L. Eddins, *Digital Image Processing Using MATLAB®, 2nd ed.* United States: Gatesmark Publishing, 2009.

[7] P. Soille, *Morphological Image Analysis: Principles and Applications*. Berlin; New York: Springer, 1999, pp. 173–174.

[8] D. Arthur and S. Vassilvitskii, "K-Means: The Advantages of Careful Seeding," in *Proceedings of the Eighteenth Annual ACM-SIAM Symposium on Discrete Algorithms*, Philadelphia, PA, USA: Society for Industrial and Applied Mathematics, 2007, pp. 1027–1035. doi: 10.5555/1283383.1283494.

[9] T. F. Chan and L. A. Vese, "Active Contours without Edges," *IEEE Transactions on Image Processing*, vol. 10, no. 2, pp. 266–277, 2001, doi: 10.1109/83.902291.

[10] S. K. Narayanan, et al., "A View on Despeckling in Ultrasound Imaging," *International Journal of Signal Processing, Image Processing and Pattern Recognition*, vol. 2, pp. 85-98, 2009.

[11] A. Rodriguez-Molares*, O. M. H. Rindal*, O. Bernard, A. Nair, M. A. Lediju Bell, H. Liebgott, A. Austeng, and L. Løvstakken, "The Ultra-Sound ToolBox," in *IEEE International Ultrasonics Symposium (IUS)*, 2017, pp. 1-4. doi: 10.1109/ULTSYM.2017.8092389.

[12] G. Montaldo, M. Tanter, J. Bercoff, N. Benech, and M. Fink, "Coherent Plane-Wave Compounding for Very High Frame Rate Ultrasonography and Transient Elastography," *IEEE Transactions on Ultrasonics, Ferroelectrics, and Frequency Control*, vol. 56, no. 3, pp. 489–506, 2009, doi: 10.1109/TUFFC.2009.1067.

[13] A. Austeng, C. C. Nilsen, A. C. Jensen, S. P. Nasholm, and S. Holm, "Coherent Plane-Wave Compounding and Minimum Variance Beamforming," in *IEEE International Ultrasonics Symposium (IUS)*, New York: IEEE, 2011, pp. 2448–2451. doi: 10.1109/ULTSYM.2011.0608.

[14] M. Albulayli and D. Rakhmatov, "Hybrid Adaptive/Nonadaptive Beamforming for Ultrasound Imaging," in *2013 IEEE International Conference on Acoustics, Speech and Signal Processing (ICASSP)*, New York, NY, USA, 2013, pp. 1061–1065. doi: 10.1109/ICASSP.2013.6637812.

[15] T. L. Szabo, "Diagnostic Ultrasound Imaging: Inside Out," in *Diagnostic Ultrasound Imaging: Inside Out*, United States: Elsevier Science & Technology, 2004.

[16] D. Go, J. Kang, I. Song, and Y. Yoo, "Efficient Transmit Delay Calculation in Ultrasound Coherent Plane-Wave Compound Imaging for Curved Array Transducers," *Applied Sciences*, vol. 9, no. 13, pp. 2752-, 2019, doi: 10.3390/app9132752.

[17] I. K. Holfort, F. Gran, and J. A. Jensen, "Broadband Minimum Variance Beamforming for Ultrasound Imaging," *IEEE Transactions on Ultrasonics, Ferroelectrics, and Frequency Control*, vol. 56, no. 2, pp. 314–325, 2009, doi: 10.1109/TUFFC.2009.1040.

[18] R. Cobbold, *Foundations of Biomedical Ultrasound*. New York, NY: Oxford University Press, 2007.

[19] F. J. Harris, "On the Use of Windows for Harmonic Analysis with the Discrete Fourier Transform," *Proceedings of the IEEE*, vol. 66, no. 1, pp. 51–83, 1978, doi: 10.1109/PROC.1978.10837.

[20] N. Otsu, "A Threshold Selection Method from Gray-Level Histograms," *IEEE Transactions on Systems, Man, and Cybernetics*, vol. 9, no. 1, pp. 62–66, 1979, doi: 10.1109/TSMC.1979.4310076.

[21] D. Bradley and G. Roth, "Adapting Thresholding Using the Integral Image," *Journal of Graphics Tools*, vol. 12, no. 2, pp. 13-21, 2007.

[22] B. D. Van Veen and K. M. Buckley, "Beamforming: A Versatile Approach to Spatial Filtering," *IEEE ASSP Magazine*, vol. 5, no. 2, pp. 4–24, 1988, doi: 10.1109/53.665.

[23] D. H. Johnson and D. E. Dudgeon, *Array Signal Processing: Concepts and Techniques*. 1993.

[24] R. E. McKeighen and M. P. Buchin, “New Techniques for Dynamically Variable Electronic Delays for Real Time Ultrasonic Imaging,” in *1977 Ultrasonics Symposium*, 1977, pp. 250–254, doi: 10.1109/ULTSYM.1977.196834.

[25] R. J. Mailloux, “Phased Array Theory and Technology,” *Proceedings of the IEEE*, vol. 70, no. 3, pp. 246–291, 1982, doi: 10.1109/PROC.1982.12285.

[26] A. Weyman, "Physical Principles of Ultrasound," in *Principles and Practice of Echocardiography*, 2nd ed., Media, PA: Williams & Wilkins, 1994.

[27] C. Otto, "Principles of Echocardiographic Image Acquisition and Doppler Analysis," in *Textbook of Clinical Echocardiography*, 2nd ed., Philadelphia, PA: WB Saunders, 2000.

[28] S. Mills and Regina Univ. (Saskatchewan). Faculty of Education, *F.Y.I. For Your Imagination [microform]: Focused Imaging. Instructional Strategies Series No. 12*, S. Mills, Distributed by ERIC Clearinghouse, Washington, D.C., 1993.

[29] J. A. Mann and W. F. Walker, "A Constrained Adaptive Beamformer for Medical Ultrasound: Initial Results," in *2002 IEEE Ultrasonics Symposium Proceedings, Vols. 1 and 2*, New York, NY, USA: IEEE, 2002, pp. 1807–1810 vol. 2. doi: 10.1109/ULTSYM.2002.1192650.

[30] M. Sasso and C. Cohen-Bacrie, “Medical Ultrasound Imaging Using the Fully Adaptive Beamformer,” in *Proceedings. (ICASSP ’05). IEEE International Conference on Acoustics, Speech, and Signal Processing, 2005*, IEEE, 2005, p. ii/489-ii/492 Vol. 2. doi: 10.1109/ICASSP.2005.1415448.

[31] F. Viola and W. F. Walker, “Adaptive Signal Processing in Medical Ultrasound Beamforming,” in *2005 IEEE Ultrasonics Symposium, Vols 1-4*, NEW YORK: IEEE, 2005, pp. 1980–1983. doi: 10.1109/ULTSYM.2005.1603264.

[32] R. M. Haralick and L. G. Shapiro, *Computer and Robot Vision*, 1st ed. USA: Addison-Wesley Longman Publishing Co., Inc., 1992, pp. 158-205.

[33] R. van den Boomgaard and R. van Balen, "Methods for Fast Morphological Image Transforms Using Bitmapped Binary Images," *CVGIP: Graphical Models and Image Processing*, vol. 54, no. 3, pp. 252–258, 1992, doi: 10.1016/1049-9652(92)90055-3.

[34] P. Soille, *Morphological Image Analysis: Principles and Applications*. Berlin; New York: Springer, 1999, pp. 164–165.

[35] I. Molnar, "Uniform Quartz - Silver Nanoparticle Injection Experiment," Digital Rocks Portal, 2016. https://www.digitalrocksportal.org/projects/44.

[36] R. Harikumar, B. Vinoth Kumar, G. Karthick, L. K. Chand, and C. Navin Kumar, “Hierarchical Clustering Algorithm for Intensity Based Cluster Merging and Edge Detection in Medical Images,” in *Proceedings of the Fourth International Conference on Signal and Image Processing 2012 (ICSIP 2012)*, India: Springer India, 2013, pp. 323–337. doi: 10.1007/978-81-322-0997-3_30.

[37] O. Yogev, A. A. Shapiro, and E. K. Antonsson, “A Novel Energy-Based Approach for Merging Finite Elements,” *International Journal for Numerical Methods in Engineering*, vol. 85, no. 2, pp. 187–205, 2011, doi: 10.1002/nme.2963.

[38] V. Caselles, R. Kimmel, and G. Sapiro, "Geodesic Active Contours," *International Journal of Computer Vision*, vol. 22, no. 1, pp. 61-79, 1997.

[39] G. Vara, A. Rustici, A. Sechi, C. Mosconi, V. Lucidi, and R. Golfieri, “Texture Analysis on Ultrasound: The Effect of Time Gain Compensation on Histogram Metrics and Gray-Level Matrices,” *Journal of Medical Physics*, vol. 45, no. 4, pp. 249–255, 2020, doi: 10.4103/jmp.jmp_82_20.

[40] H. L. V. Trees, *Optimum Array Processing*. New York, NY: Wiley, 2002.

[41] M. F. Schiffner and G. Schmitz, “Frequency-Dependent F-Number Suppresses Grating Lobes and Improves the Lateral Resolution in Coherent Plane-Wave Compounding,” *IEEE Transactions on Ultrasonics, Ferroelectrics, and Frequency Control*, vol. 70, no. 9, pp. 1101–1117, 2023, doi: 10.1109/TUFFC.2023.3291612.

[42] M. F. Schiffner and G. Schmitz, "Frequency-Dependent F-Number Increases the Contrast and the Spatial Resolution in Fast Pulse-Echo Ultrasound Imaging," in *International Ultrasonics Symposium (IEEE IUS 2021)*, New York, NY, USA, 2021, doi: 10.1109/IUS52206.2021.9593488.

[43] H. Liebgott, A. Rodriguez-Molares, F. Cervenansky, J. A. Jensen, and O. Bernard, "Plane-Wave Imaging Challenge in Medical Ultrasound," in *2016 IEEE International Ultrasonics Symposium (IUS)*, Tours, France, 2016, pp. 1-4, doi: 10.1109/ULTSYM.2016.7728908.

[44] K. He, X. Zhang, S. Ren, and J. Sun, “Deep Residual Learning for Image Recognition,” in *2016 IEEE Conference on Computer Vision and Pattern Recognition (CVPR)*, New York, NY, USA, 2016, pp. 770–778, doi: 10.1109/CVPR.2016.90.

[45] S. Ren, K. He, R. Girshick, and J. Sun, “Faster R-CNN: Towards Real-Time Object Detection with Region Proposal Networks,” *arXiv.org*, 2016, doi: 10.48550/arxiv.1506.01497.

[46] J. Redmon, S. Divvala, R. Girshick, and A. Farhadi, "You Only Look Once: Unified, Real-Time Object Detection," in *2016 IEEE Conference on Computer Vision and Pattern Recognition (CVPR)*, New York, NY, USA, 2016, pp. 779–788. doi: 10.1109/CVPR.2016.91.

[47] W. Liu et al., "SSD: Single Shot MultiBox Detector," in *Computer Vision - ECCV 2016, Pt I*, vol. 9905, Cham: Springer International Publishing, 2016, pp. 21–37. doi: 10.1007/978-3-319-46448-0_2.

[48] Y. Chen, X. Yuan, R. Wu, J. Wang, Q. Hou, and C. Ming-Ming, “YOLO-MS: Rethinking Multi-Scale Representation Learning for Real-time Object Detection,” *arXiv.org*, 2023, doi: 10.48550/arxiv.2308.05480.

[49] Y. Zhong, J. Wang, J. Peng, and L. Zhang, “Anchor Box Optimization for Object Detection,” in *2020 IEEE Winter Conference on Applications of Computer Vision (WACV)*, IEEE, 2020, pp. 1275–1283. doi: 10.1109/WACV45572.2020.9093498.

[50] J. Hosang, R. Benenson, and B. Schiele, "Learning Non-Maximum Suppression," *arXiv.org*, 2017. doi: 10.48550/arxiv.1705.02950.

[51] C. Ma, C.-Y. Yang, X. Yang, and M.-H. Yang, "Learning a No-Reference Quality Metric for Single-Image Super-Resolution," *Computer Vision and Image Understanding*, vol. 158, pp. 1–16, 2017, doi: 10.1016/j.cviu.2016.12.009.

[52] S. M. Pizer, R. E. Johnston, J. P. Ericksen, B. C. Yankaskas, and K. E. Muller, "Contrast-Limited Adaptive Histogram Equalization: Speed and Effectiveness," in *[1990] Proceedings of the First Conference on Visualization in Biomedical Computing*, IEEE Comput. Soc. Press, 1990, pp. 337–345. doi: 10.1109/VBC.1990.109340.